Monthly Notices of the ROYAL ASTRONOMICAL SOCIETY

MNRAS **520,** 4258–4275 (2023) https://doi.org/10.1093/mnras/stad252
Advance Access publication 2023 January 27

Self-regulation of black hole accretion via jets in early protogalaxies

Kung-Yi Su,[1,2,3]★ Greg L. Bryan,[1,2] Zoltán Haiman,[2] Rachel S. Somerville,[3] Christopher C. Hayward[3] and Claude-André Faucher-Giguère[4]

[1]*Black Hole Initiative, Harvard University, 20 Garden Street, Cambridge, MA 02138, USA*
[2]*Department of Astronomy, Columbia University, 550 West 120th Street, New York, NY 10027, USA*
[3]*Center for Computational Astrophysics, Flatiron Institute, 162 Fifth Avenue, New York, NY 10010, USA*
[4]*Department of Physics & Astronomy and CIERA, Northwestern University, 1800 Sherman Ave, Evanston, IL 60201, USA*

Accepted 2023 January 18. Received 2022 December 23; in original form 2022 July 21

ABSTRACT

The early growth of black holes (BHs) in high-redshift galaxies is likely feedback regulated. While radiative feedback has been extensively studied, the role of mechanical feedback has received less scrutiny to date. Here, we use high-resolution parsec-scale hydrodynamical simulations to study jet propagation and its effect on 100 $M_\odot$ BH accretion in the dense, low-metallicity gas expected in early protogalaxies. As the jet propagates, it shocks the surrounding gas forming a jet cocoon. The cocoon consists of a rapidly cooling cold phase at the interface with the background gas and an overpressured subsonic phase of reverse shock-heated gas filling the interior. We vary the background gas density and temperature, BH feedback efficiency, and the jet model. We found that the width of the jet cocoon roughly follows a scaling derived by assuming momentum conservation in the jet-propagation direction and energy conservation in the lateral directions. Depending on the assumed gas and jet properties, the cocoon either stays elongated to large radii or isotropizes before reaching the Bondi radius, forming a nearly spherical bubble. Lower jet velocities and higher background gas densities result in self-regulation to higher momentum fluxes and elongated cocoons. In all cases, the outward cocoon momentum flux balances the inward inflowing gas momentum flux near the Bondi radius, which ultimately regulates BH accretion. The time-averaged accretion rate always remains below the Bondi rate, and exceeds the Eddington rate only if the ambient medium is dense and cold, and/or the jet is weak (low velocity and mass loading).

Key words: accretion, accretion discs – black hole physics – hydrodynamics – methods: numerical – galaxies: jets.

1 INTRODUCTION

The origin of supermassive black holes (SMBHs) with masses of $\gtrsim 10^9$ $M_\odot$, powering bright quasars observed in the first billion years after the big bang (redshifts $z \gtrsim 6$; see e.g. Bosman 2022 for an up-to-date compilation) remains an unsolved puzzle. Proposed explanations range from rapid, super-Eddington growth of stellar-mass seed black holes (BHs), the 'direct collapse' of a supermassive star, to runaway mergers between stellar-mass objects, as well as more exotic phenomena (see e.g. Inayoshi, Visbal & Haiman 2020; Volonteri, Habouzit & Colpi 2021, for recent comprehensive reviews).

One promising scenario is for a low-mass seed BH to grow at rates well above the fiducial Eddington rate $\dot{M}_{\rm Edd} \equiv L_{\rm Edd}/\epsilon c^2$ (where $L_{\rm Edd}$ is the Eddington luminosity, c is the speed of light, and ϵ is a radiative efficiency). Indeed, small-scale simulations of BH accretion show that BHs surrounded by dense gas can accrete at rates up to at least $\sim 100\ \dot{M}_{\rm Edd}$ (e.g. Jiang, Stone & Davis 2014; Sadowski et al. 2014). However, feedback from the BH accretion itself poses possible obstacles to sustaining such rapid growth. Even in the presence of dense ambient gas, allowing rapid fuelling, radiative feedback on large scales tends to make the accretion episodic, with a strongly suppressed time-averaged accretion rate (e.g. Milosavljević et al. 2009; Park & Ricotti 2011). BH radiation may also outright eject gas from the shallow gravitational potential of its low-mass parent halo, preventing rapid accretion (Alvarez, Wise & Abel 2009). On the other hand, these deleterious radiative effects may be avoided in the hyper-Eddington regime, in which radiation is trapped and cannot exert large-scale feedback (Inayoshi, Haiman & Ostriker 2016; Takeo, Inayoshi & Mineshige 2020).

In addition to radiative feedback, mechanical feedback presents another potential obstacle to rapid and sustained BH growth. While such mechanical feedback has been less explored in the high-redshift context, it is well established to play a crucial role in galaxy formation and evolution at lower redshifts. Active galactic nucleus (AGN) feedback is known to quench star formation in massive galaxies and clusters, keeping them 'red and dead' over a significant fraction of cosmic time. Among the different forms of AGN feedback, extensive galaxy-scale simulations have shown that AGN jet models are, in principle, capable of quenching a galaxy and stopping the cooling flows (e.g. Dubois et al. 2010; Gaspari, Brighenti & Temi 2012; Yang, Sutter & Ricker 2012; Li & Bryan 2014; Li et al. 2015; Prasad, Sharma & Babul 2015; Yang & Reynolds 2016; Bourne & Sijacki 2017; Ruszkowski, Yang & Zweibel 2017; Martizzi et al. 2019; Su et al. 2020). Observational studies also infer that AGNs can provide an energy budget comparable to the cooling rate (Bîrzan et al. 2004). There are also observations of unambiguous cases of AGNs expelling

★ E-mail: kungyisu@gmail.com

gas from galaxies, injecting thermal energy via shocks or sound waves, via photoionization and Compton heating, or via 'stirring' the circumgalactic medium (CGM) and intracluster medium (ICM). This can create 'bubbles' of hot plasma with non-negligible relativistic components, which are ubiquitous around massive galaxies (see e.g. Fabian 2012; Hickox & Alexander 2018, for a detailed review). In Su et al. (2021) and Su et al. (in preparation), we carried out a broad parameter study of AGN jets in $10^{12}-10^{15}\,M_\odot$ clusters and found a subset of models which inflate a sufficiently large cocoon with a long enough cooling time that these jets can quench the central galaxy.

In addition to the thoroughly studied cases of SMBHs in massive galaxies, various studies also suggested AGN feedback in much smaller dwarf galaxies and from intermediate-mass BHs ($M_{\rm acc}\sim 10^2-10^5\,M_\odot$; Nyland et al. 2017; Bradford et al. 2018; Penny et al. 2018; Dickey et al. 2019; Manzano-King, Canalizo & Sales 2019), some of which are observed in the form of AGN jets (e.g. Greene, Ho & Ulvestad 2006; Wrobel & Ho 2006; Wrobel et al. 2008; Mezcua & Lobanov 2011; Nyland et al. 2012; Reines & Deller 2012; Webb et al. 2012; Mezcua et al. 2013a, b, 2015, 2018a, b; Reines et al. 2014;Mezcua, Suh & Civano 2019). Unsurprisingly, AGN feedback can also affect the growth of these smaller BHs, alter the surrounding gas properties, and play a significant role in sculpting the galaxy they live in, especially in dwarfs and high-redshift galaxies (Wellons et al. 2022). Eventually, a self-regulating scenario of accretion and jet propagation might occur (e.g. López-Cámara, De Colle & Moreno Méndez 2019).

Observations also find SMBHs ($M_{\rm acc}\gg 10^5\,M_\odot$) at high-redshift ($z\gtrsim 4$) with jetted AGN quasars (e.g. Sbarrato et al. 2021, 2022). It is unclear whether a $\sim$100 $M_\odot$ BH, which can be presumed to produce jets, as well, if it is fed at super-Eddington rates, could sustain rapid growth on to an SMBH. Recent work has addressed this problem in slightly different contexts, either investigating the impact of wider-angle outflows produced at larger radii in the accretion flow (e.g. Takeo et al. 2020), or by utilizing galaxy-scale simulations to assess the growth of larger BHs ($>10^4\,M_\odot$) with a jet (e.g. Regan et al. 2019; Massonneau et al. 2022). This work aims to study how AGN jets affect accretion on to $100\,M_\odot$ 'seed' BHs in dense, low-metallicity gas, mimicking conditions expected in high-redshift protogalaxies. Additionally, we study in detail the physics of how jet-inflated cocoons propagate to large radii and self-regulate BH accretion, using analytic models to interpret our simulation results.

In galaxy-scale simulations, including in our own previous work (e.g. Su et al. 2020, 2021; Torrey et al. 2020; Wellons et al. 2022), both AGN feedback and BH accretion have been implemented with sub-grid prescriptions. Models based on Bondi–Hoyle accretion (Bondi 1952; Springel, Di Matteo & Hernquist 2005) and accretion via gravitational torques (Hopkins & Quataert 2011; Anglés-Alcázar et al. 2017) involve assumptions about gas properties, which might not always be valid, especially in the presence of an unresolved jet. To better address this question, in this work, we model a cloud of gas with systematically varied properties around the BH at sufficiently high resolution (with the minimum gravitational force softening at least 1000 times less than the Bondi radius), to resolve the gravitational capture of individual gas particles (Hopkins et al. 2016; Anglés-Alcázar et al. 2021).[1] We also implement various jet models to study how they affect BH accretion and how the jet propagates to a larger radius. Although the jets in this study are launched at a much smaller scale, the initial jet itself remains sub-grid relative to the scales we can resolve. This work also addresses how sub-grid jet models launched on different scales connect to each other. We also parametrize the results of our simulations in order to provide the effective long-term time-averaged accretion rate, given different gas properties beyond the Bondi radius and with different jet models. We delineate the parameter space of gas and jet properties over which super-Eddington growth may occur.

The rest of this paper is organized as follows. In Section 2, we summarize our initial conditions (ICs), BH accretion model, and the AGN jet parameters we survey, and we describe our numerical simulations. We present the results with different jet velocities, which show the most dramatic differences, in Section 3. We develop a toy model describing the regulation of different jet models in different environments in Section 4. We present a suite of additional simulations with varying model parameters and compare the results with the toy model in Section 5. We compare our study to several other recent works, and summarize the implications of our findings in Section 6. We enumerate our main conclusions in Section 7. We include a set of simulations exploring numerical choices, as well as resolution studies, in Appendix A.

2 METHODOLOGY

We perform simulations of a box of gas under the effect of jet feedback from a 100 $M_\odot$ BH. Our simulations use GIZMO[2] (Hopkins 2015), in its meshless finite mass (MFM) mode, which is a Lagrangian mesh-free Godunov method, capturing advantages of both grid-based and smoothed-particle hydrodynamics (SPH) methods. Numerical implementation details and extensive tests are presented in a series of methods papers for, e.g. hydrodynamics and self-gravity (Hopkins 2015). All of our simulations employ the FIRE-2 implementation of cooling (followed from 10 to 10^{10}K), including the effects of photoelectric and photoionization heating, collisional, Compton, fine-structure, recombination, atomic, and molecular cooling (following Hopkins et al. 2018). Note that we impose a temperature floor at T_∞, which will be specified in the ICs (and systematically varied), assuming other feedback processes not included in these simulations keep the gas from cooling further. We assume a metallicity of $10^{-4}\,Z_\odot$, which may be expected in the protogalaxies hosting the first stellar-mass BH seeds, and which is sufficiently low that metal cooling above 10^3 K (the lowest value of T_∞ that we adopt) is negligible.

2.1 Initial conditions

Ideally, we would evolve the BH accretion within the context of a cosmological simulation that resolves the gas dynamics at high redshift (e.g. as done for minihaloes by Alvarez et al. 2009). However, given the very large uncertainties in high-redshift conditions, we instead approximate the physical conditions near the BH as a uniform patch of gas, in order to model the centre of an atomic cooling halo. This allows us to systematically vary the gas properties in order to understand how these impact the BH regulation. In particular, the IC we adopt is a uniform 3D-box of uniformly distributed gas particles with constant density and temperature, which we denote n_∞ and T_∞. A 100 $M_\odot$ BH is placed at the centre of the box. As mentioned above, the initial metallicity of the gas is set to a very low value ($10^{-4}\,Z_\odot$).

[1] The exact fueling in the accretion disc depends on unresolved plasma physics (e.g. Cho & Narayan 2022) and remains sub-grid.

[2] A public version of this code is available at http://www.tapir.caltech.edu/~phopkins/Site/GIZMO.html.

To achieve a higher resolution in the vicinity of the BH, where the accretion occurs and the overall regulation is determined, and in the vicinity of the jet, we use a hierarchical super-Lagrangian refinement scheme (Su et al. 2020, 2021) to reach $\sim 1.4 \times 10^{-6}\,M_\odot (n_\infty/10^4\,\mathrm{cm^{-3}})$ mass resolution around the z-axis where the jet is launched, much higher than many previous global studies (e.g. Weinberger et al. 2017; Su et al. 2021). The mass resolution decreases as a function of distance from the z-axis (r_{2d}), roughly proportional to r_{2d} for $r_{2d} > 2.5 \times 10^{-2}$ pc. The numerical details are summarized in Table 1. The highest resolution region is where r_{2d} is smaller than $r_{2d} = 2.5 \times 10^{-3}$ pc unless otherwise stated. A resolution study is presented in Appendix A.

2.2 BH accretion

As discussed in the introduction, BH accretion is not modelled with the Bondi assumption, but instead is determined by following the gravitational capture of gas (Hopkins et al. 2016; Anglés-Alcázar et al. 2021) directly, and implementing its subsequent accretion on to the BH via an α-disc prescription (see below). A gas particle is accreted if it is gravitationally bound to the BH and the estimated apocentric radius is smaller than r_{acc}.[3] This sink radius r_{acc} is set to 3×10^{-5} to 1.5×10^{-4} pc according to the BH neighbourhood gas density. In more detail, the sink radius r_{acc} is set to be a radius from the BH enclosing 96 'weighted' neighborhood gas particles but capped to be within (3×10^{-5} to 1.5×10^{-4} pc).

Although we follow the gas down to distances very close to the BH, we do not model the accretion disc itself, but instead adopt a simple α-disc model. The accreted gas adds to the α-disc mass (M_α, which is initially set to zero). The mass in the α-disc is then supplied to the BH at the rate

$$\dot{M}_{acc} = M_\alpha / t_{disc}. \quad (1)$$

We assume a constant $t_{disc} = 1000$ yr from an estimated viscous time-scale of a Shakura & Sunyaev (1973) disc, assuming the accretion disc is at 10^4 K, as $t_{disc} \sim t_{ff}\mathcal{M}^2/\alpha \sim 1000\,\mathrm{yr}\,(M_{acc}/100\,M_\odot)^{1/2}\,(\alpha/0.1)^{-1}\,\left(r_{acc}/10^{-4}\mathrm{pc}\right)^{1/2}$, where t_{ff} is the free-fall time at r_{acc} and $\mathcal{M}$ is the Mach number of gas in the α-disc. In Appendix A, we explore the impact of varying t_{disc}.

2.3 Jet models

We adopt a jet model following Su et al. (2021). In brief, a jet is launched with a particle-spawning method, which creates new gas cells ('resolution elements') to represent the jet material. The spawned particles have a fixed initial mass, temperature, and velocity, which sets the specific energy of the jet. With this method we have better control of the jet properties, as launching using particle spawning depends less on local gas properties than when depositing energy/momentum based on the distribution of neighboring gas elements.[4] We can also enforce a higher resolution for the jet elements, allowing light jets to be accurately modelled. The spawned gas particles have a mass resolution as indicated in Table 1 and are forbidden to de-refine (merge into a common gas element) before they decelerate to 10 per cent of the launch velocity. Two particles are spawned in opposite z-directions at the same time when the accumulated jet mass flux reaches twice the target spawned particle mass, so linear momentum is always exactly conserved. Initially, the spawned particle is randomly placed on a sphere with a radius of r_0, which is either 10^{-5} pc or half the distance between the BH and the closest gas particle, whichever is smaller. If the particle is initialized at a position (r_0, θ_0, ϕ_0) in spherical polar coordinates, and the jet opening-angle of a specific model is θ_{op} (say $= 1^\circ$, which is the case for our jet model), the polar angle of the initial velocity direction of the jet will be set at $\theta_v = 2\theta_{op}\theta_0/\pi$. With this, the projected paths of any two particles will not intersect.

We parametrize the jet mass flux with a constant feedback mass fraction

$$\dot{M}_{jet} = \eta_{m,fb}\dot{M}_{acc}, \quad (2)$$

so the feedback energy and momentum fluxes are

$$\dot{E}_{jet} = \eta_{m,fb}\dot{M}_{acc}\left(\frac{1}{2}V_{jet}^2 + \frac{3kT_{jet}}{2\mu}\right),$$
$$\dot{P}_{jet} = \eta_{m,fb}\dot{M}_{acc}V_{jet}, \quad (3)$$

where V_{jet} is the adopted jet velocity and μ is the mean particle mass. Initially, the jet has a negligible thermal component ($T_{jet} = 10^4$ K). We emphasize that this is the velocity and mass loading at our jet-launching scale in the simulation, which is several orders of magnitude larger than the gravitational radius. The adopted velocity and $\eta_{m,fb}$ depends on details which we do not resolve, such as plasma physics processes involving the interaction of jet and gas, so we leave them as free parameters. As we will show later, the formation of the pressurized cocoon is a result of shock heating of the jet with the surrounding gas. We tested $\eta_{m,fb}$ from 0.005 to 100. Most of the runs adopt $\eta_{m,fb} = 0.05$, but as we will show in our result later, the jet fluxes are what actually get regulated and $\eta_{m,fb}$ just decides how much the BH should accrete to achieve such a flux. Our ignorance of the true value of this parameter means that the actual growth rate of the BH is not well constrained by our results (although the jet properties are).

3 TWO MODES OF JET PROPAGATION

Before exploring all of the simulations that we have run, we first focus on a set of three simulations all with the same fiducial background gas properties ($n_\infty = 10^4\,\mathrm{cm^{-3}}$ and $T_\infty = 10^4$ K) and feedback mass fraction ($\eta_{m,fb} = 0.05$), but varying the jet velocity, ranging from 3000 to 30 000 km s^{-1}. These models are denoted as 'η5e-2–vj3e3–n1e5–T1e4', 'η5e-2–vj1e4–n1e5–T1e4' (I,II,III), and 'η5e-2–vj3e4–n1e5–T1e4'. These velocity variations result in very different jet cocoons and, as we will see, guide our development of a simple model which will explain how the jet evolves when we modify other parameters (such as the background gas properties).

3.1 Cocoon morphology

Fig. 1 shows the morphology of the cocoon for the three different jet velocities, depicting the resulting density and temperature distributions. In this work, we refer to the cocoon as the whole pressurized region shock-heated by the jet. Note that, in these figures, the hot jet gas is most clearly visible, but this is surrounded by a region of shocked ambient material. We use the term 'cocoon' to refer to the combination of both regions. The BH accretion and resulting jet are

[3]This provides a scale for the sub-grid accretion model and for the α-disc model.

[4]The traditional method usually does a particle neighbour search from the BH and dumps the designated energy and momentum into these gas particles. Therefore, the effect will depend on the local gas properties and the exact geometric distribution. See Wellons et al. (2022) for a comparison of different methods.

Table 1. Physics variations of all simulations.

Model	Numerical details				Feedback parameters			Efficiency		Background gas		Resulting averaged accretion rate and fluxes			
	ΔT	Box size	$m_{\rm g}^{\rm max}$	$m_{\rm jet}$	$\eta_{\rm m,\,fb}$	$V_{\rm jet}$	$T_{\rm jet}$	$\eta_{\rm P}$	$\eta_{\rm E}$	n_∞	T_∞	$\langle\dot{M}_{\rm acc}\rangle$	$\frac{\langle\dot{M}_{\rm acc}\rangle}{\dot{M}_{\rm Bondi}}$	$\frac{\langle\dot{M}_{\rm acc}\rangle}{\dot{M}_{\rm Edd}}$	$\frac{\langle\dot{E}_{\rm jet}\rangle}{\dot{E}_{\rm Edd}}$
	(kyr)	(pc)	($M_\odot$)	($M_\odot$)		(km s^{-1})	(K)			(cm^{-3})	(K)	($M_\odot\,yr^{-1}$)			
Fiducial															
η5e-2–vj1e4–n1e5–T1e4 (I,II,III)[a]	100	0.4	1.4e-6	1e-7	0.05	1e4	1e4	1.6e-3	2.7e-5	1e5	6e3	0.7-1.5e-7	2.1-4.6e-3	0.031-0.067	0.87-1.9e-5
Feedback mass fraction															
η5e-3–vj1e4–n1e5–T1e4	100	0.4	1.4e-6	1e-7	0.005	1e4	1e4	1.6e-4	2.7e-6	1e5	6e3	9.4e-7	2.9e-2	0.42	1.2e-5
η5e-1–vj1e4–n1e5–T1e4	100	0.4	1.4e-6	1e-7	0.5	1e4	1e4	1.6e-2	2.7e-4	1e5	6e3	1.3e-8	4e-4	5.8e-3	1.6e-5
η1e2–vj1e4–n1e5–T1e4	100	0.4	1.4e-6	1e-7	99	1e4	1e4	3.3	5.5e-2	1e5	6e3	7.1e-11	2,2e-6	3.2e-5	8.9e-8
Jet velocity															
η5e-2–vj3e3–n1e5–T1e4	90	0.8	1.4e-6	1e-7	0.05	3e3	1e4	5e-4	2.5e-6	1e5	6e3	1e-5	0.31	4.5	1.1e-4
η5e-2–vj3e4–n1e5–T1e4	100	0.4	1.4e-6	1e-7	0.05	3e4	1e4	5e-3	2.5e-4	1e5	6e3	8.9e-9	2.7e-4	4.0e-3	1e-5
Thermal jet															
η5e-2–Tj3e9–n1e5–T1e4	100	0.4	1.4e-6	1e-7	0.05	3e3	3e9	5e-4	2.7e-5	1e5	6e3	2.4e-8	7.4e-4	0.011	3.0e-6
Gas density															
η5e-2–vj3e3–n1e2–T1e4	100	0.4	1.4e-9	1e-10	0.05	1e4	1e4	1.6e-3	2.7e-5	1e2	6e3	1.6e-11	4.9e-4	7.2e-6	2e-9
η5e-2–vj3e3–n1e3–T1e4	100	0.4	1.4e-8	1e-9	0.05	1e4	1e4	1.6e-3	2.7e-5	1e3	6e3	2.3e-10	7.0e-4	1.0e-4	2.9e-8
η5e-2–vj3e3–n1e4–T1e4	100	0.4	1.4e-7	1e-8	0.05	1e4	1e4	1.6e-3	2.7e-5	1e4	6e3	3.5e-9	1.1e-3	1.6e-3	4.4e-7
η5e-2–vj3e3–n1e6–T1e4	40	0.8	1.4e-5	1e-6	0.05	1e4	1e4	1.6e-3	2.7e-5	1e6	6e3	1.3e-5	4e-2	5.8	1.6e-3
Gas temperature															
η5e-2–vj3e3–n1e5–T1e3	50	3.2	1.4e-6	1e-7	0.05	1e4	1e4	1.6e-3	2.7e-5	1e4	6e3	1.9e-6	4.2e-3	0.85	2.4e-4
η5e-2–vj3e3–n1e5–T1e5	12	0.08	1e-8	8e-10	0.05	1e4	1e4	1.6e-3	2.7e-5	1e4	1e5	4.4e-9	3.0e-2	2.0e-3	5.5e-7

Notes. This is a partial list of simulations studied here with different jet and background gas parameters. The columns list: (1) Model name: The naming of each model starts with the feedback mass fraction, followed by the jet velocity in km s^{-1} for kinetic jet or jet temperature in K for thermal dominant jet. The final two numbers labels the background gas density in cm^{-3} and background gas temperature in K. (2) ΔT: Simulation duration (all shorter than the free-fall time for constant n_∞ gas without a BH). (3) Box size of the simulation. (4) $m_{\rm g}^{\rm max}$: The highest mass resolution. (5) $m_{\rm jet}^{\rm max}$: The mass resolution of the spawned jet particles. (6) $\eta_{\rm m,\,fb}$: The feedback mass fraction. (7) $V_{\rm jet}$: The initial jet velocity at spawn. (8) $T_{\rm jet}$: The initial jet temperature at spawn. (9) $\eta_{\rm p}$: The feedback momentum efficiency ($\dot{P}_{\rm jet}/\dot{M}_{\rm jet}c$). (10) $\eta_{\rm p}$: The feedback energy efficiency ($\dot{E}_{\rm jet}/\dot{M}_{\rm jet}c^2$). (11) n_∞: The background gas density. (12) T_∞: The background gas temperature. (13) $\langle\dot{M}_{\rm acc}\rangle$: The resulting time-averaged accretion rate (at the endpoint in Fig. 2). (14) $\langle\dot{M}_{\rm acc}\rangle/\dot{M}_{\rm Bondi}$: The same value over Bondi accretion rate. (15) $\langle\dot{M}_{\rm acc}\rangle/\dot{M}_{\rm Edd}$: The same value over the Eddington accretion rate ($\dot{M}_{\rm Edd}\equiv\dot{L}_{\rm Edd}/0.1c^2$). (16) $\langle\dot{E}_{\rm jet}\rangle/\dot{E}_{\rm Edd}$: Jet energy flux over Eddington luminosity. [a]We run three variations of the same run with different random seeds for the stochastic injection of jet particles (labelled as I, II, III) to characterize the impact of this stochasticity. Unless specified otherwise, in the rest of this paper we refer to run I.

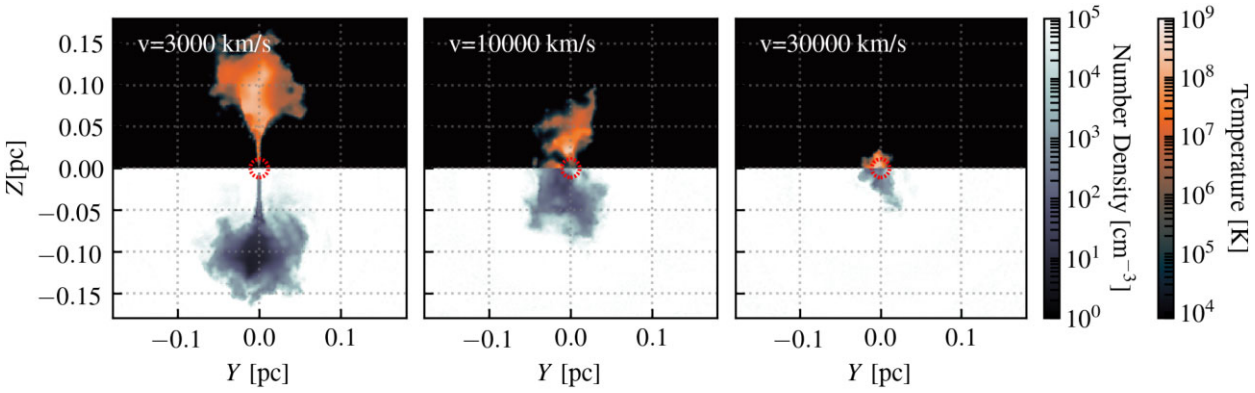

Figure 1. The number density (lower half of each panel) and temperature (upper half of each panel) morphology of the runs varying the jet velocity from 3000 to 30 000 km s^{-1} (η5e-2–vj3e3–n1e5–T1e4, η5e-2–vj1e4–n1e5–T1e4, and η5e-2–vj3e3–n1e5–T1e4) and keeping everything else constant. We show 2D slices from 3D snapshots, selected at the time when the cocoon has reached its maximum height. The red dotted circle indicates the Bondi radius in each panel. We see that low jet velocities result in elongated cocoons, while high velocities produce a more spherical bubble-like morphology, and propagate to a shorter distance.

highly episodic (see Fig. 2), and as a result, the length and the width of the jet cocoon are also time-dependent. We choose a snapshot where each cocoon reaches its maximum height in order to show the differences most clearly. This figure shows that the propagation of the jet cocoon varies primarily in length. The run with a lower jet velocity has a much more elongated jet cocoon, reaching a much larger distance. On the other hand, the higher velocity runs result in a roughly isotropic bubble-shaped cocoon. The higher the velocity, the shorter the distance the jet cocoon reaches.

Qualitatively, this is primarily because a lower velocity jet with lower specific energy regulates itself to a higher mass and momentum flux (for reasons we will discuss below). The higher mass and momentum flux jet can punch through to a much larger radius, consistent with what we see in galaxy scale jet simulations (e.g. Krause 2003; Guo 2015; Su et al. 2021; Weinberger et al. 2022). We will provide a more quantitative scaling for the propagation of the jet cocoon with jet models and the initial external gas density and temperature in Section 4.

These jet cocoons reach only ~ 0.1 pc scales. We emphasize that these are generated by a 100 $M_\odot$ BH and should not be directly compared with the jet cocoon or bubble from an SMBH, which can reach several tens of kpc. As we will discuss later (Section 5.5) in the derived scaling from a simple model we develop, an SMBH will imply much higher jet fluxes and will reach much further in a similar environment.

3.2 Black hole accretion rate and jet energy flux

Fig. 2 shows the resulting BH accretion rate, jet mass flux, momentum flux, and energy flux as a function of time for the same set of runs. The latter quantity is the cumulative-average from the beginning of the run $t = 0$ to the given time to reduce the noise. With a feedback mass fraction of $\eta_{\rm m,\,fb} = 0.05$, the BH accretion rate roughly regulates to $2\dot{M}_{\rm bond}$, $\sim 0.02 - 0.03\dot{M}_{\rm bond}$, and $\sim 0.002\dot{M}_{\rm bond}$ for jet velocities of 3000, 10 000, and 30 000 km s^{-1}, respectively. We also see that the higher the jet velocity, the more short-term variability there is throughout the simulations (a period of $\sim$3, 10, 50 kyr, respectively), a topic we will return to in Section 5.6.

Consistent with what we saw in Section 3.1, a low-velocity jet regulates to a much higher mass and momentum flux, which is responsible for the more elongated cocoon. The 10 000 and 30 000 km s^{-1} runs, both of which have cocoons that isotropize at small radius, roughly regulate to a similar jet energy flux, meaning that $\dot{M}_{\rm jet} \propto V_{\rm jet}^{-\kappa_v}$ with $\kappa_v \sim 2$–2.5. The lowest velocity run (3000 km s^{-1}), on the other hand, results in an even higher energy flux, qualitatively consistent with the much larger volume of the cocoon we see in Fig. 1. The lower velocity runs ($V_{\rm jet} \leq 10\,000$ km s^{-1}) roughly have $\dot{M}_{\rm jet} \propto V_{\rm jet}^{-\kappa_v}$, with $\kappa_v \sim 3.5$–4. We will explore the reason behind the different behaviour and scalings of the high and low velocity jets in the next section.

4 A SIMPLE MODEL FOR JET PROPAGATION AND COCOON FORMATION

In the previous section, we found that when we varied the jet velocity, the jets all self-regulated, but this could result either in a nearly spherical, or in a highly elongated cocoon. Here, we develop a simple analytic model based on this dichotomy and then, in the next section, we will use it to understand self-regulation when other parameters, such as the background gas properties, are changed.

4.1 Jet propagation

We begin by reviewing the scaling which controls the cocoon shape before, in the next section, connecting this back to the accretion and hence overall self-regulation.

4.1.1 Elongated jet cocoon – before the cocoon isotropizes

We start by assuming the jet cocoon roughly follows a cylindrical geometry. As shown in Fig. 3, closer to where jets are launched, the propagation of the jet qualitatively follows from momentum conservation in the z-direction (e.g. Begelman & Cioffi 1989; Su et al. 2021),

$$A_c V_z \rho_\infty V_z = \frac{1}{2}\dot{M}_{\rm jet} V_{\rm jet}, \tag{4}$$

where $A_c = \pi R_{\rm cocoon}^2$ is the cross-section of the pressurized cylinder (cocoon), $V_z \equiv {\rm d}z_{\rm cocoon}/{\rm d}t$ is the expansion velocity of the cocoon in the polar directions, $\dot{M}_{\rm jet}$ is the jet's initial mass flux, and $V_{\rm jet}$ is the initial jet velocity.

The evolution in the perpendicular direction is, instead, dictated by energy conservation, as the build-up of an overpressured cocoon drives lateral expansion. The resulting expansion then pushes the

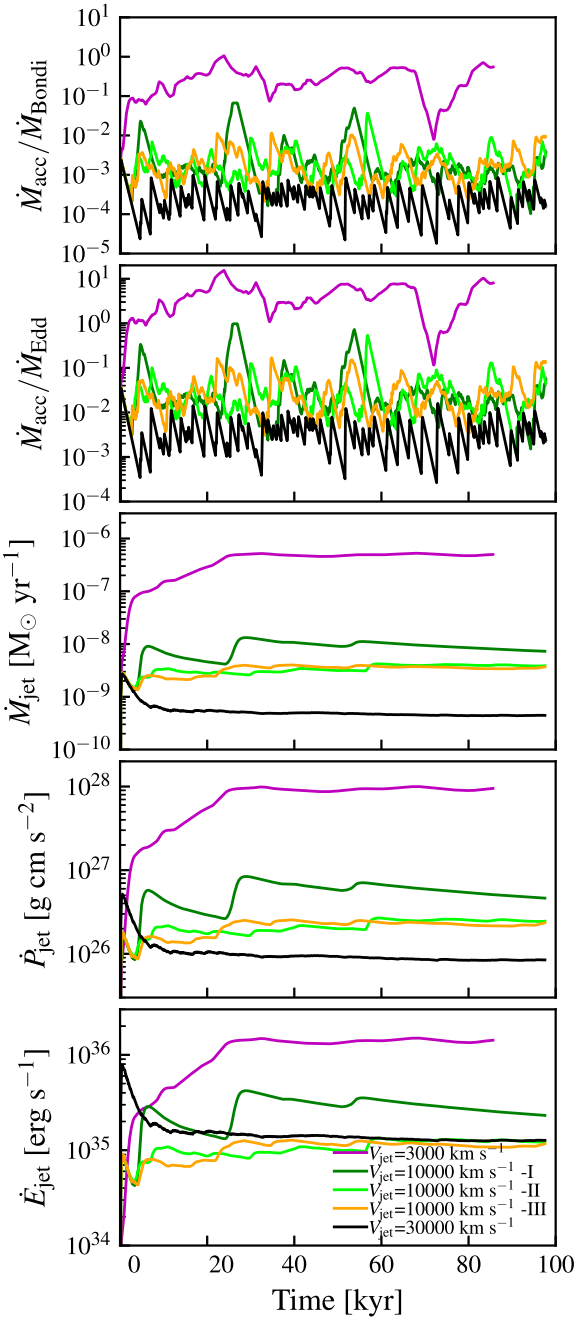

Figure 2. From top to bottom, the panels show (i, ii) the BH accretion rate, (iii) jet mass flux, (iv) momentum flux, and (v) energy flux in runs varying the jet velocity from 3000 to 30 000 km s^{-1} (labelled as 'η5e-2–vj3e3–n1e5–T1e4', 'η5e-2–vj1e4–n1e5–T1e4', and 'η5e-2–vj3e3–n1e5–T1e4' in Table 1). Note that I, II, and III in the name label the same runs with different random seeds to show the range of stochastic variations. The second, third, and fourth panels show cumulative averages from the beginning of the run up to the specific time of the run. The lower velocity jet model results in a much higher BH accretion rate and jet mass, momentum, and energy fluxes. The higher velocity jets (10 000 and 30 000 km s^{-1}) regulate themselves to a similar jet energy flux values.

surrounding gas. The equations describing the conservation of energy and momentum flux can be written as

$$A_{\rm tot} V_{R,\rm Hot}\left(\frac{1}{2}\rho_c V_{R,\rm Hot}^2\right) = \frac{\gamma}{2}(\dot{M}_{\rm jet} V_{\rm jet}^2),$$
$$V_{R,\rm Hot}^2 \rho_c = V_R^2 \rho_\infty \quad (5)$$

where $A_{\rm tot} = 4\pi\beta R_{\rm cocoon} z_{\rm cocoon}$ is the lateral surface area of the same region, $z_{\rm cocoon}$ is the height to which the jet reaches, $V_{R,\rm Hot}$ is the immediate post-shock velocity of the hot cocoon gas, $V_R \equiv {\rm d}R_{\rm cocoon}/{\rm d}t$ is the expansion velocity of the cocoon in the mid-plane direction, β is an order-of-unity geometric factor for the surface area of the cocoon with respect to an ideal cylindrical geometry, and $\gamma \equiv \dot{E}_{\rm expansion}/\dot{E}_{\rm kin} \propto \dot{E}_{\rm jet}/\dot{E}_{\rm kin} \equiv f_{\rm kin}^{-1}$ is the ratio of the energy flux in the perpendicular direction (proportional to the total injected energy $\dot{E}_{\rm jet}$) to the injected kinetic energy flux. Energy conservation is appropriate for the (initial) lateral expansion despite the strong cooling that can occur at the interface between the hot and cold gas within the cocoon. The total amount of cooling at this interface is proportional to its area (i.e. A_c) and so is negligible compared with the jet energy flux at early times.

In this expression, $\rho_{\rm c}$ is the cocoon gas density, which we will assume depends on the jet velocity and the background gas properties as

$$\rho_c \propto \rho_\infty^\zeta T_\infty^\xi V_{\rm jet}^\delta. \quad (6)$$

where ζ, ξ, and δ are exponents that we will determine later. Assuming the cocoon is pressurized by strong shocks (where $\rho_{\rm post} \sim 2\rho_{\rm pre}$ and $v_{\rm post} \sim 0.5 v_{\rm pre}$), γ is roughly

$$\gamma_{\rm super-sonic} \sim \frac{\dot{E}_{\rm post-shock}}{\dot{E}_{\rm pre-shock}}\frac{\dot{E}_{\rm pre-shock}}{\dot{E}_{\rm jet}}\frac{\dot{E}_{\rm jet}}{\dot{E}_{\rm kin}}$$
$$\sim \frac{\rho_{\rm post} v_{\rm post}^3}{\rho_{\rm pre} v_{\rm pre}^3} \times (1 - f_{\rm loss}) f_{\rm kin}^{-1}$$
$$\sim \frac{1}{16} \times (1 - f_{\rm loss}) f_{\rm kin}^{-1} \lesssim \frac{1}{16} f_{\rm kin}^{-1}. \quad (7)$$

Therefore, we assume γ is a constant for the remainder of the paper.

From the equations above, we can solve for the time dependence of V_R and $R_{\rm cocoon}$ as

$$V_R = \left(\frac{\gamma^2}{72\pi\beta^2}\right)^{1/6} \dot{M}_{\rm jet}^{1/6} \rho_c^{1/6} \rho_\infty^{-1/3} V_{\rm jet}^{1/2} t^{-1/3}$$
$$R_{\rm cocoon} = \left(\frac{81\gamma^2}{512\pi\beta^2}\right)^{1/6} \dot{M}_{\rm jet}^{1/6} \rho_c^{1/6} \rho_\infty^{-1/3} V_{\rm jet}^{1/2} t^{2/3} \quad (8)$$

and the time dependence of V_z and $z_{\rm cocoon}$ as

$$V_z = \left(\frac{8\beta}{9\pi\gamma}\right)^{1/3} \dot{M}_{\rm jet}^{1/3} \rho_c^{-1/6} \rho_\infty^{-1/6} t^{-2/3}$$
$$z_{\rm cocoon} = \left(\frac{24\beta}{\pi\gamma}\right)^{1/3} \dot{M}_{\rm jet}^{1/3} \rho_c^{-1/6} \rho_\infty^{-1/6} t^{1/3}. \quad (9)$$

In particular, the opening angle of the resulting cocoon scales as

$$\frac{R_{\rm cocoon}}{z_{\rm cocoon}} = \frac{\gamma z_{\rm cocoon}}{16\beta}\left(\frac{2\pi\rho_c V_{\rm jet}}{\dot{M}_{\rm jet}}\right)^{1/2}. \quad (10)$$

We have assumed that the jet starts such that $R_{\rm cocoon} < z_{\rm cocoon}$, but as the cocoon propagates, for a fixed $\dot{M}_{\rm jet}$, eventually, it becomes

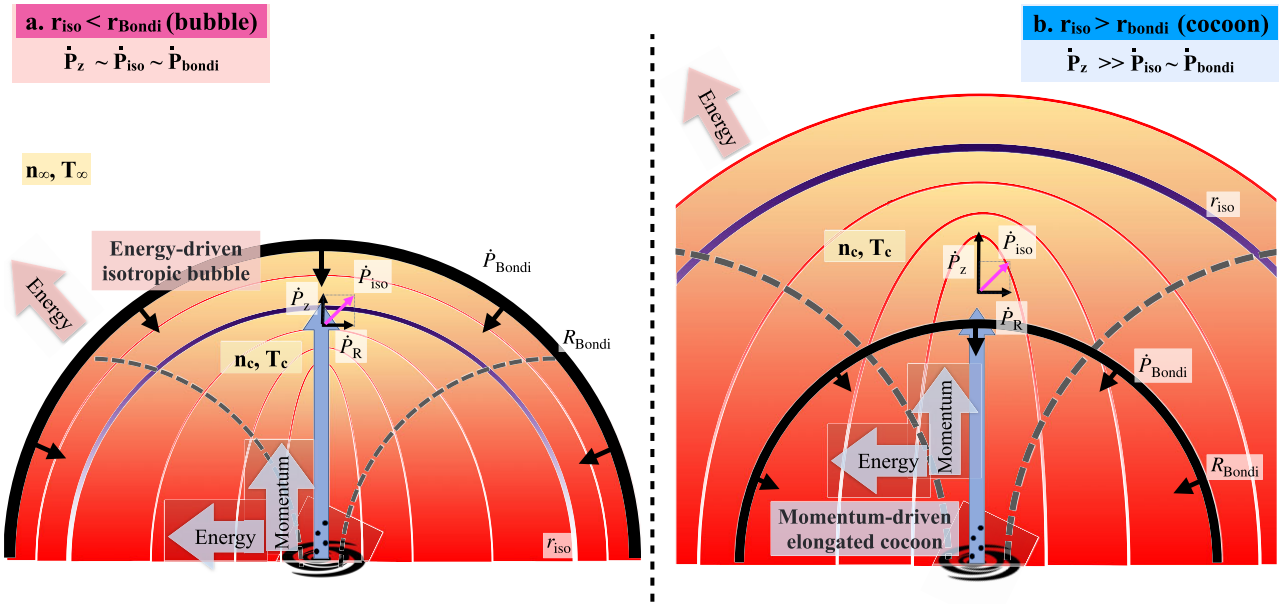

Figure 3. A cartoon picture of the jet cocoon propagation and the two possible cocoon morphologies as a result of different jet parameters, background gas density, and temperature. The left-hand panel shows the isotropic 'bubble' case where $r_{\rm iso} < r_{\rm Bondi}$. The right-hand panel shows the elongated 'cocoon' case where $r_{\rm iso} > r_{\rm Bondi}$. The blue arrow represents the jet. Each half oval indicates the jet cocoon at a given time. The grey dashed line indicates the resulting overall effective cocoon shape of a continuous jet injection by 'linking' the cocoon shock-front at each time.

(quasi-)isotropic ($R_{\rm cocoon} \sim z_{\rm cocoon}$); this occurs at a time given by

$$t_{\rm iso} = \left(\frac{2^{15}\dot{M}_{\rm jet}\rho_\infty}{\pi V_{\rm jet}^3 \rho_c^2}\right)^{1/2}\left(\frac{\beta^2}{3\gamma^2}\right)$$
$$\approx 660\,{\rm yr} \times (1-f_{\rm loss})^{-2} f_{\rm kin}^2 \left(\frac{\bar{n}}{10^5\,{\rm cm^{-3}}}\right)^{-1/2}$$
$$\times \left(\frac{\dot{M}_{\rm jet}}{5\times10^{-9}\,{\rm M_\odot\,yr^{-1}}}\right)^{1/2}\left(\frac{V_{\rm J}}{10^4\,{\rm km\,s^{-1}}}\right)^{-3/2}, \quad (11)$$

and at a cocoon height of (see Fig. 3)

$$z_{\rm iso} \equiv r_{\rm iso} = \left(\frac{\dot{M}_{\rm jet}}{2\pi\rho_c V_{\rm jet}}\right)^{1/2}\left(\frac{16\beta}{\gamma}\right)$$
$$\approx 1.3\times10^{-3}\,{\rm pc}\ (1-f_{\rm loss})^{-1} f_{\rm kin} \times \left(\frac{\bar{n}}{10^5\,{\rm cm^{-3}}}\right)^{-1/2}$$
$$\times \left(\frac{\dot{M}_{\rm jet}}{5\times10^{-9}\,{\rm M_\odot\,yr^{-1}}}\right)^{1/2}\left(\frac{V_{\rm J}}{10^4\,{\rm km\,s^{-1}}}\right)^{-1/2}. \quad (12)$$

4.1.2 *Isotropic bubble – after the cocoon isotropizes*

After the cocoon isotropizes, the momentum no longer dominates the jet propagation as V_R grows larger than V_z. The whole cocoon becomes an energy-driven expanding bubble as shown in the outer part of Fig. 3. In this case,

$$4\pi R^2 \rho_c V_{R,\rm Hot}^3 = \frac{\gamma'}{2}\dot{M}_{\rm jet}V_{\rm jet}^2$$
$$V_{R,\rm Hot}^2 \rho_c = V_R^2 \rho_\infty, \quad (13)$$

where $\gamma' \equiv \dot{E}_{\rm expansion}/\dot{E}_{\rm kin}$. Note that this matches equation (5) assuming $R_{\rm cocoon} = z_{\rm cocoon}$ up to an order-of-unity geometry factor, which we treat in a very approximate manner. Again assuming supersonic shocks, then $\gamma' \sim \gamma_{\rm supersonic}$. Equation (13) has the solution:

$$V_{\rm R} = \left(\frac{9\gamma'\dot{M}_{\rm jet}V_{\rm jet}^2\rho_c^{1/2}}{200\pi\rho_\infty^{3/2}}\right)^{1/5}(t-t_{\rm iso})^{-2/5}$$
$$R = \left(\frac{125\gamma'\dot{M}_{\rm jet}V_{\rm jet}^2\rho_c^{1/2}}{216\pi\rho_\infty^{3/2}}\right)^{1/5}(t-t_{\rm iso})^{3/5}. \quad (14)$$

4.2 Feedback self-regulation

Turning to the physics of self-regulation, we note that, at the Bondi radius $R_{\rm Bondi} = GM_{\rm acc}/c_s^2$, the inflowing mass flux goes as

$$\dot{M}_{\rm Bondi} = \frac{e^{3/2}\pi\rho_\infty G^2M^2}{c_s^3} \quad (15)$$

and the inflowing momentum flux goes as

$$\dot{P}_{\rm Bondi} = \dot{M}_{\rm Bondi}V_{\rm ff}|_{R_{\rm Bondi}} = \frac{e^{3/2}\pi\rho_\infty G^2M_{\rm acc}^2}{c_s^2}. \quad (16)$$

Regulation will occur when the jet cocoon produces a momentum flux which matches this. However, if the momentum flux is very anisotropic such that the z component of momentum flux $\dot{P}_{z,\rm cocoon}$ is much larger than the momentum flux perpendicular to the jet $\dot{P}_{\rm R,cocoon}$, the extra momentum in the z-direction is insufficient, by itself, to stop the accretion. Therefore, we argue that regulation happens when the isotropic component of the jet cocoon or bubble momentum flux matches the inflowing momentum flux at the Bondi radius.

$$4\pi\rho_\infty R_{\rm Bondi}^2 V_{\rm iso,Bondi}^2 = \frac{e^{3/2}\pi\rho_\infty G^2M_{\rm acc}^2}{c_s^2}, \quad (17)$$

where $V_{\rm iso,\,Bondi}$ is the isotropic component of the cocoon velocity at the Bondi radius. We estimate the isotropic component of the cocoon velocity as $V_{\rm iso} \equiv \sqrt{2}\min(V_R, V_Z)$. We explain how we estimate its value under different conditions as follows.

4.2.1 $z_{iso} > \mathrm{R}_{Bondi}$

As shown in the right-hand part of Fig. 3, if the jet cocoon isotropizes at a radius larger than the Bondi radius ($z_{\rm iso} > R_{\rm Bondi}$), $V_z > V_R$ when R reaches $R_{\rm Bondi}$, we estimate the isotropic component of velocity at the Bondi radius to be

$$V_{\rm iso,Bondi} = \sqrt{2} V_R|_{R_{\rm Bondi}} \propto \dot{M}_{\rm jet}^{1/4} V_{\rm jet}^{3/4} R_{\rm Bondi}^{-1/2} \rho_c^{1/4} \rho_\infty^{-1/2}. \quad (18)$$

From equations (17) and (18), we find that the jet mass flux regulates to

$$\dot{M}_{\rm jet} \propto M_{\rm acc}^2 \rho_\infty^2 \rho_c^{-1} V_{\rm jet}^{-3} \propto M_{\rm acc}^2 \rho_\infty^{2-\zeta} T_\infty^{-\xi} V_{\rm jet}^{-3-\delta}. \quad (19)$$

4.2.2 $z_{iso} < \mathrm{R}_{Bondi}$

On the other hand, as shown in the left-hand part of Fig. 3, if $z_{\rm iso} < R_{\rm Bondi}$, the cocoon can also become an isotropic bubble before reaching the Bondi radius. Therefore, equation (13) in this case gives

$$V_{\rm iso,Bondi} = \left(\frac{\gamma' \dot{M}_{\rm jet} V_{\rm jet}^2 \rho_c^{1/2}}{8\pi \rho_\infty^{3/2} R_{\rm Bondi}^2} \right)^{1/3}. \quad (20)$$

From equations (17) and (20), we see that the jet mass flux in this case regulates to

$$\dot{M}_{\rm jet} \propto M_{\rm acc}^2 \rho_\infty^{3/2} \rho_c^{-1/2} V_{\rm jet}^{-2} c_s^{-1} \propto M_{\rm acc}^2 \rho_\infty^{(3-\zeta)/2} V_{\rm jet}^{-2-\delta/2} T_\infty^{-(1+\xi)/2}. \quad (21)$$

4.3 Cocoon or bubble at the Bondi Radius?

The jet cocoon will be elongated at the Bondi radius if $z_{\rm iso} > R_{\rm Bondi}$ or, from equation (12), if

$$\dot{M}_{\rm jet} > \left(\frac{\pi \gamma^2 R_{\rm Bondi}^2}{128 \beta^2} \right) \rho_c V_{\rm jet} \sim \rho_\infty^{\zeta} T_\infty^{\xi} V_{\rm jet}^{1+\delta}. \quad (22)$$

Otherwise, it isotropizes before reaching the Bondi radius. We next list which of these two scenarios is realized for different parameter values, as follows.

(i) **Jet velocity:** This mass flux criterion scales as $V_{\rm jet}$, but the mass fluxes are regulated to a negative power of $V_{\rm jet}$ in both the cocoon (equation 19) and bubble (equation 21) cases, as δ is small (as we measured in simulation). Therefore the lower the jet velocity, the narrower the cocoon at the Bondi radius. We emphasize that the 'jet velocity', $V_{\rm jet}$ here is the velocity at the jet launching scale in our simulation, $\sim 10^{-5}$ pc, which is six orders of magnitude larger than the Schwarzschild radius. This velocity therefore strongly depends not only on the unresolved launching of a relativistic jet but also on the interaction between the jet and the gas on an unresolved scale. We will discuss this further in Section 6.3.

(ii) **Gas density:** If ζ (from equation 6) is smaller than 1 (which is the case, as will be shown later in Section 5.2), then $\dot{M}_{\rm jet}$ has a superlinear dependence on n_∞ for both the elongated cocoon and isotropic bubble cases. The separation between the two cases, on the other hand, has $\dot{M}_{\rm jet}$ scaling linearly with n_∞ (equation 22). From the same argument as above, the higher the background density, the more elongated the jet cocoon.

(iii) **Gas temperature:** If ξ (from equation 6) is close to zero (which is the case as will be shown later in Section 5.2), the $\dot{M}_{\rm jet}$ in the elongated cocoon case will have little dependence on T_∞, while the bubble case will have a scaling of $\dot{M}_{\rm jet} \propto T_\infty^{-0.5}$. The separation between the two cases has a negligible dependence of $\dot{M}_{\rm jet}$ on T_∞, (equation 22). From the same argument above, if the background temperature increases, the cocoon shape either remains the same or becomes slightly more bubble-like.

5 SIMULATION RESULTS: COCOON REGULATION AND BLACK HOLE ACCRETION

Armed with a better understanding of the physics of jet regulation from the simple scalings obtained in the previous section, we next turn to a more complete examination of the simulation results. We begin by demonstrating that the isotropic momentum is key to self-regulation, before discussing first the cocoon's properties, and then the BH accretion rate and growth.

5.1 The self-regulation of the cocoon by its isotropic momentum flux

We first explicitly demonstrate that, in the simulations, the isotropic component of the cocoon momentum flux (as defined in equations 18 and 20) is roughly regulated to the inflow momentum flux, assuming a Bondi value. We note that the 'regulation' is a dynamic process and happens on average at the Bondi radius according to the background gas properties rather than the cocoon gas properties. The reason is that most accretion happens while the jet is off (not at its maximum fluxes), when the gas around the BH becomes cold again. Each row in Fig. 4 shows the variation of a specific parameter ($\dot{M}_{\rm jet}$, $v_{\rm jet}$, n_∞, T_∞, and $T_{\rm jet}$). There are three kinds of momentum flux plotted in each panel. The first is the injected jet momentum, time-averaged over the duration of each run, which is coloured red.

The second kind of momentum flux is the time-averaged cocoon momentum flux. The blue line shows its total value, the pink line the isotropic component, and the cyan line the z component. More specifically, we define the cocoon momentum flux by summing the gas particles as

$$\begin{aligned} \langle P_{\rm out} \rangle &= \sum_{r_i = r \pm \delta r, T_i > 1.2 T_\infty, v_{r,} > 0} \frac{m_i v_{r,i}^2}{\delta r} \\ \langle P_{\rm out,z} \rangle &= \sum_{r_i = r \pm \delta r, T_i > 1.2 T_\infty, v_{z,i} \cdot sign(z) > 0} \frac{m_i v_{z,i}^2}{\delta r} \\ \langle P_{\rm out,R} \rangle &= \sum_{r_i = r \pm \delta r, T_i > 1.2 T_\infty, v_{r2d,i} > 0} \frac{m_i v_{r2d,i}^2}{\delta r} \\ \langle P_{\rm out,iso} \rangle &= \min(P_{\rm out}, 2P_{\rm out,R}, 2P_{\rm out,z}), \end{aligned} \quad (23)$$

where m_i is the particle mass, T_i is the temperature, r_i is the particle's 3D radial position, $v_{r,i}$ is the 3D radial velocity, $v_{z,i}$ is the z-velocity, and $v_{r2d,i}$ is the lateral velocity.

The third kind of momentum flux is the estimated inflowing momentum flux assuming a Bondi density profile

$$\rho \sim \begin{cases} \rho_\infty & \text{for} r > R_{\rm Bondi} \\ \rho_\infty \left(\frac{r}{R_{\rm Bond}} \right)^{-3/2} & \text{for} r < R_{\rm Bondi} \end{cases} \quad (24)$$

multiplied by the $4\pi r^2 v_{\rm ff}^2$. Note that $v_{\rm in} \sim V_{\rm ff}$ does not hold far beyond $R_{\rm Bondi}$, so we only plot this curve out to $\sim 3R_{\rm Bondi}$. We immediately see that the isotropic component of the momentum flux (pink curves) is roughly regulated to the Bondi inflowing momentum flux (green curves) at the Bondi radius (vertical line) (within a factor of 2). More specifically, the runs can be separated into two categories – $z_{\rm iso} > R_{\rm Bondi}$ (cocoon-like at $R_{\rm Bondi}$) and $z_{\rm iso} < R_{\rm Bondi}$ (bubble-like at $R_{\rm Bondi}$).

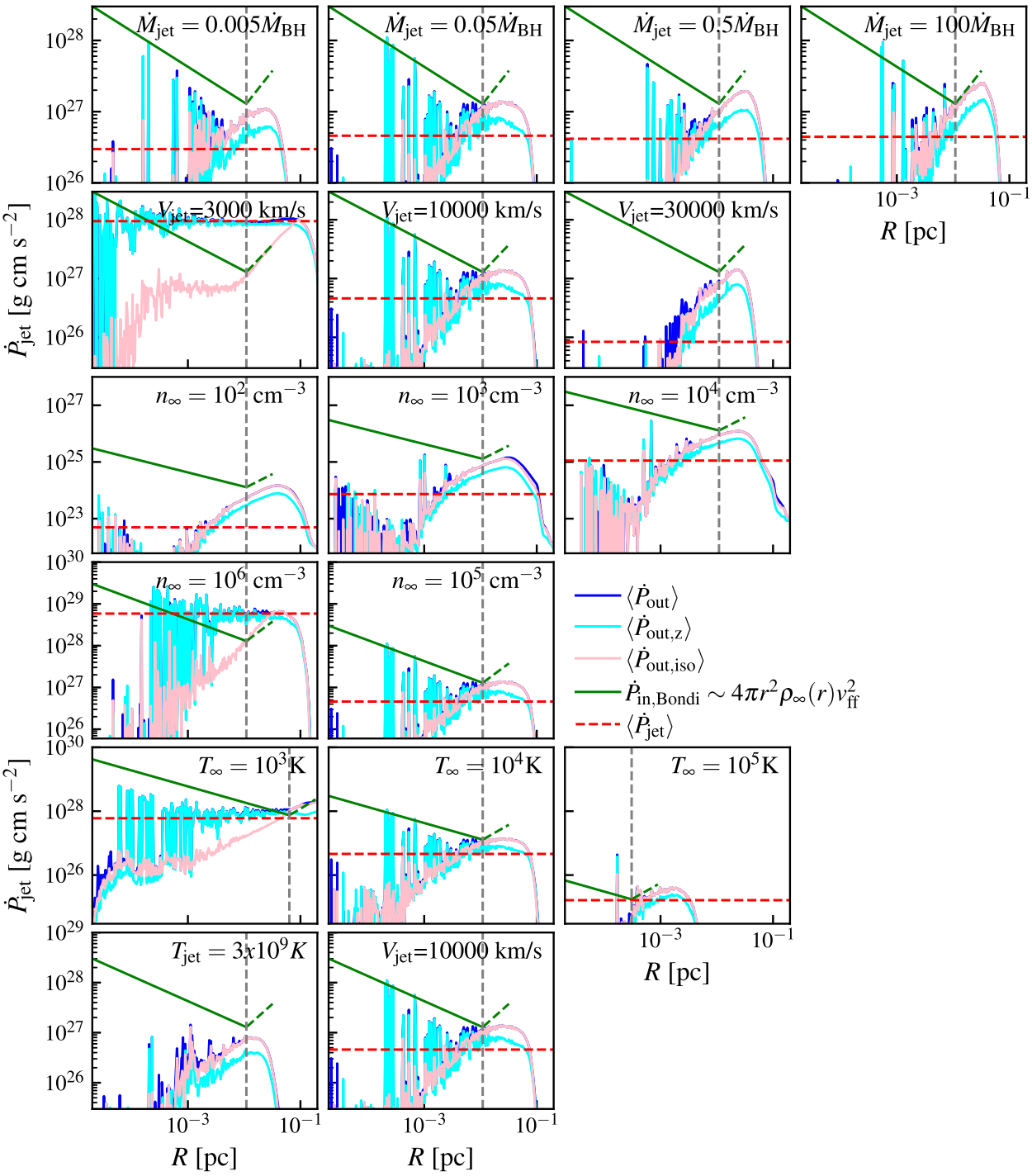

Figure 4. The comparison of time-averaged momentum fluxes from the simulations. Three types of momentum flux are shown: (i) the average jet momentum flux (red), (ii) the cocoon momentum flux, with blue, cyan, and pink lines showing the total cocoon flux, its z-component, and the isotropic component ($\min(\dot{P}_{\rm out}, 2\dot{P}_{\rm out,R}, 2\dot{P}_{\rm out,z})$, see equation 23 and Fig. 3), respectively, and (iii) finally the estimated inward Bondi momentum flux (green). The vertical line in each plot marks the Bondi radius. The isotropic component of the outward cocoon momentum flux matches the inward Bondi momentum flux at the Bondi radius. Runs with elongated cocoons ($v = 3000$ km s^{-1} and $n = 10^6$ cm^{-3}) have the z-component of their cocoon fluxes roughly match the jet momentum fluxes (momentum-driven) and are much larger than the isotropic components. Runs with bubble-shaped cocoons all have their cocoon momentum fluxes (energy-driven) higher than the jet momentum fluxes.

Cross-referencing the morphological plots in Fig. 1 (for the simulations with jet velocity variation) and Fig. 5 (for the simulations varying n_∞, T_∞, and $T_{\rm jet}$), both the 3000 km s^{-1} and $n = 10^6$ cm^{-3} runs fall clearly in the first category (elongated cocoons). In these runs, the z-direction momentum flux is roughly equivalent to the jet momentum flux, indicating a momentum-conserving propagation. Both are much larger than the isotropic component of the cocoon momentum flux until well beyond the Bondi radius, where the two

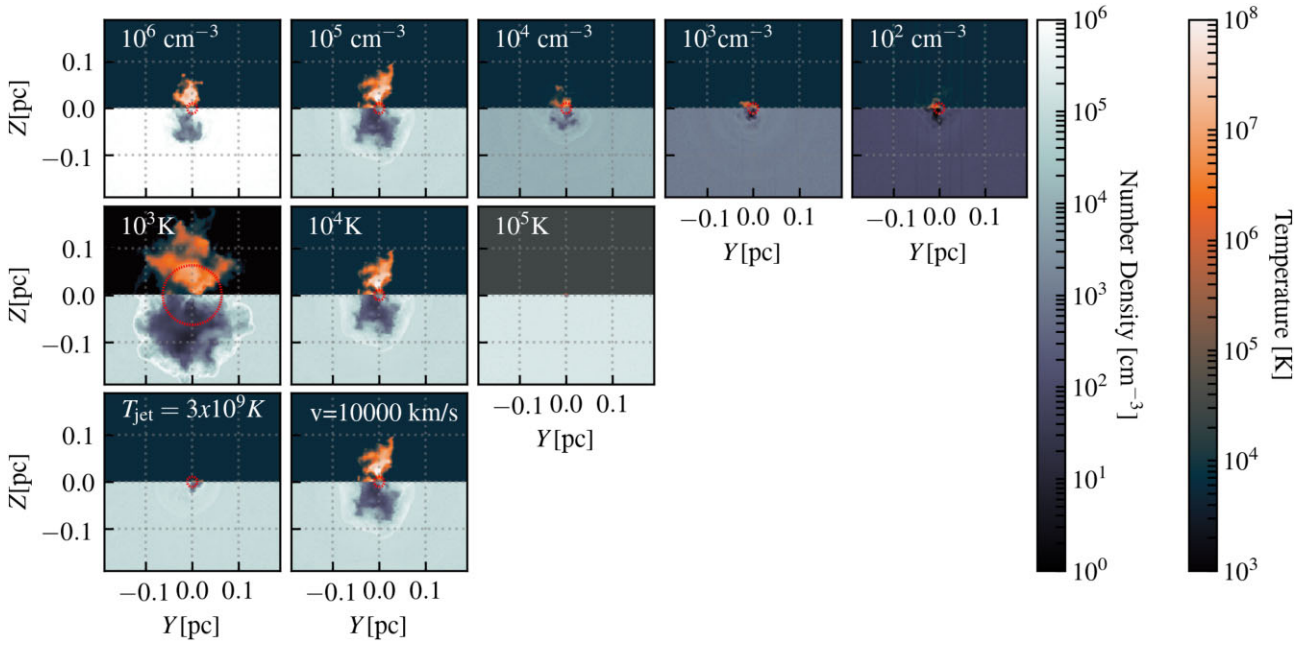

Figure 5. The density and temperature morphology of the other runs varying the other parameters. Higher density runs have much larger and more elongated jet cocoons. Lower temperature runs have a much larger Bondi radius, so the cocoon also reaches further. A thermal energy dominant jet results in a quasi-spherical bubble-shaped cocoon.

components become comparable. The z-direction momentum flux is also larger than the inflowing momentum flux (assuming a Bondi value) at the Bondi radius. The isotropic component of the cocoon momentum flux, on the other hand, matches the inflowing momentum flux. In fact, they not only match at the Bondi radius, but they also match until the jet cocoon isotropizes, at a several times larger distance. This is primarily because the isotropic component of the velocity roughly scales as $r^{-1/2}$ (see equation 18), identical to the scaling of the free-fall velocity.

The higher velocity runs ($V_{\rm jet} > 10000\,{\rm km\,s^{-1}}$), lower density runs ($n_\infty \lesssim 10^4\,{\rm cm^{-3}}$) and thermal jet runs clearly fall in the second category (see also Figs 1 and 5). In this scenario, the cocoon isotropizes at a radius much smaller than the Bondi radius, and the isotropic component and the z-component become comparable over most of the plotted range. They are both larger than the input jet momentum flux as the propagation is energy-driven (i.e. by the thermal velocity, rather than the jet's bulk velocity; see Section 4.1). However, they still match the inflowing momentum flux assuming the Bondi value.

The regulation of the isotropic component of the cocoon momentum flux to the Bondi value at $R_{\rm Bondi}$ is clearly reproduced in these results. When changing the background gas temperature by two orders of magnitude, the Bondi radius also differs by two orders of magnitude, and the two values still match.

5.2 Thermal phase structure of the cocoon/bubble gas

Before jumping into the implications of this regulation for BH accretion, we will first need to understand how the cocoon phase structure depends on the jet model and gas properties. This is reflected in the power-law index in equation (6) and enters the regulation of the jet mass flux and accretion rate in equations (19) and (21).

Fig. 6 shows the phase structure of the fiducial run η5e-2–vj1e4–n1e5–T1e4 in the temperature – $V_{\rm iso}$ (isotropic component of cocoon velocity) plane. The top panel is mass-weighted, showing the phase distribution, while the bottom panel is momentum-flux-weighted, showing which phase contributes the most to the outflowing momentum flux. There are clearly two phases present as labelled by the horizontal lines. The first is the hot phase, which consists of the reverse-shocked hot gas filling the volume of the cocoon, and is primarily trans- to subsonic-turbulent. The second, colder, phase is roughly at the background gas temperature and density and slightly above the cooling floor. The gas in this phase is at the 'mixing layer' of the cocoon and surrounding gas, which is already cold. The second panel shows that both phases have a roughly equivalent contribution to the outflowing cocoon momentum flux, while most of the mass is in the cold phase.

Fig. 6 shows that the cocoon gas has properties different from the background gas. Fig. 7 shows an estimate of how the cocoon gas properties depend on the background gas properties at the Bondi radius, where the regulation happens. This is represented as ζ and ξ in equation (6). We note that the dependence on the jet velocity is weak ($\delta \sim 0$), so we do not explicitly show it here. Given what we saw in Fig. 6, we fit for the gas properties of the whole cocoon (estimated as $T > 1.2\,T_\infty$, shown with green lines), the cool-mixing-layer phase ($1.2\,T_\infty < T < 3.6\,T_\infty$; blue lines), and the hot cocoon gas ($T > 3.6\,T_\infty$; red lines). We include only gas with $V_{\rm iso} > 0$. While averaging the cocoon gas properties, we volume-weighted the density and pressure while mass-weighting the temperature and entropy. We emphasize that this yields only an approximate estimate of the power-law index, as each jet model goes through multiple cycles of feedback and the cocoon consists of multiphase gas. To look at overall behaviour, we average over all times and the multiphase cocoon gas at the Bondi radius, and fit a straight line through the results (in logarithmic quantities).

We see from the left-hand panel that the cold-mixing-layer gas generally follows the background gas temperature and density. On the other hand, the hot cocoon gas follows a constant entropy trend, as the reverse-shock heated gas has its properties set largely by

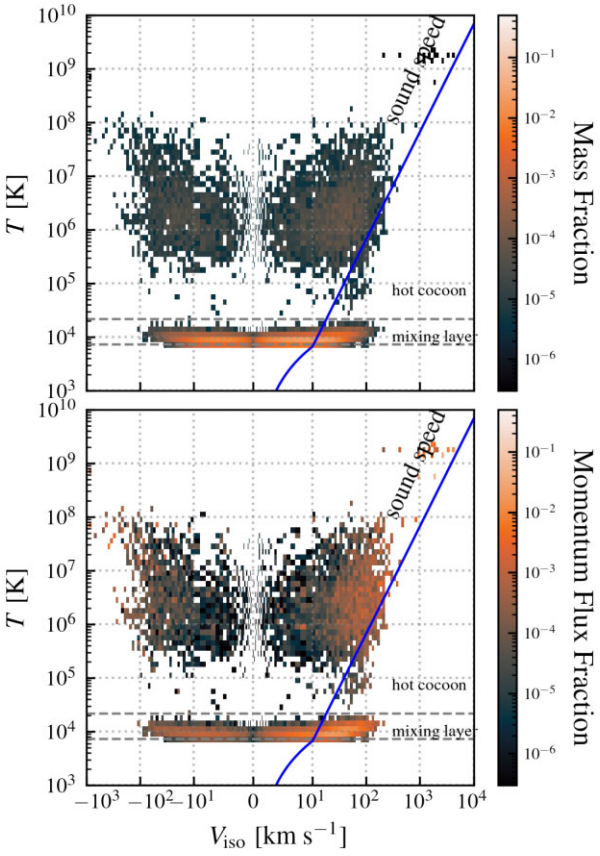

Figure 6. The phase structure of the cocoon gas ($T > 1.2\,T_\infty$) in the temperature versus isotropic velocity component plane ($V_{\rm iso} \sim \sqrt{2}V_{\rm 2d}$). The top panel is mass-weighted, and the lower panel is momentum-flux-weighted (isotropic component). The cocoon consists of a reverse-shocked, trans- to subsonic, turbulent hot phase and a cold mixing layer phase slightly above the cooling floor (labelled by the horizon lines). The two phases contribute roughly equally to the isotropic cocoon momentum flux. Most of the mass, on the other hand, is in the cold phase. The hottest temperatures roughly correspond to the shock temperature implied by the jet velocity.

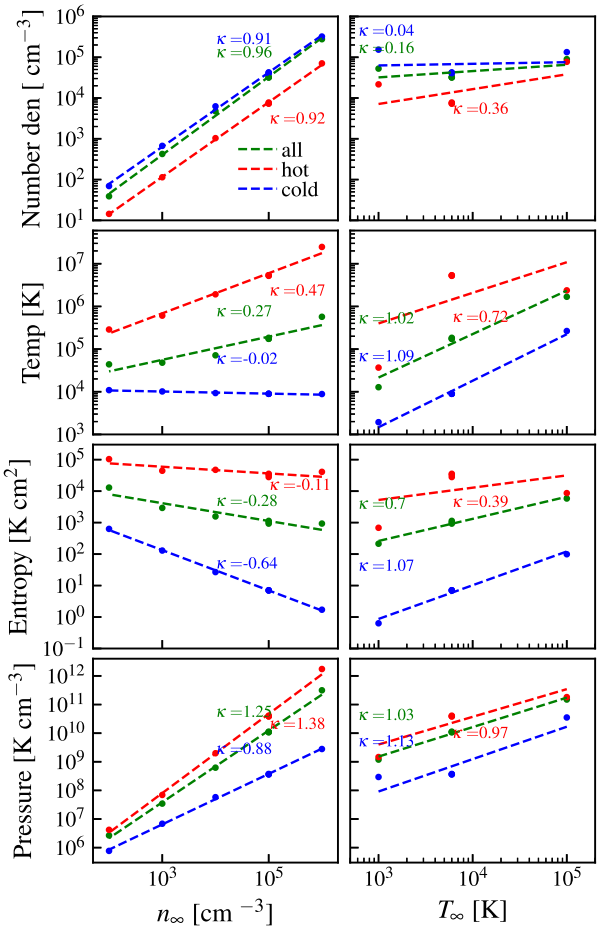

Figure 7. The dependence of the cocoon gas density, temperature, entropy, and pressure on background gas properties (the former evaluated at the Bondi radius). The red, blue, and green dots and lines correspond to the hot, cold, and combined phases. The dots are from each simulation and the lines are fitted power laws with the index (κ) labelled. The cocoon is defined for simplicity as all gas with $T > 1.2T_\infty$. We find $n_c \propto n_\infty^\zeta T_\infty^\xi$ with $\zeta \lesssim 0.9$ and $\xi \sim 0$.

the jet model instead of the background gas properties. We find a scaling approximately $n_c \propto n_\infty^\zeta$ with $\zeta \lesssim 0.9$, consistent with our claim in Section (ii) that the higher the background density, the more elongated the cocoon.

The right-hand panel shows that the cocoon gas, in either phase, scales only weakly with the background temperature. Again, the cold-mixing-layer gas roughly matches the background gas temperature since they have both already cooled to the temperature floor (T_∞). On the other hand, the hot phase has a steeper than linear scaling with the background temperature. Overall, we find a scaling of $n_c \propto T_\infty^\xi$ with $\xi \lesssim 0$. This is also roughly consistent with our claim in Section (iii) that, if ξ is smaller than 0, the higher the background temperature, the more 'isotropic' the jet cocoon (Section (iii)).

5.3 The black hole accretion rate and jet mass flux

Having determined how the cocoon properties depend on the background gas density and temperature, we can finally see whether the implied regulation of our jet and the resulting BH accretion rate in our simple model can qualitatively explain what we see in the simulations. Fig. 8 shows the time-averaged jet mass flux in all of the runs, with each panel showing the variation of a specific parameter. We plot only the jet mass flux for ease of comparison with our simple model, but it should be kept in mind that this is directly proportional to the BH accretion rate (simply scaled by a constant factor $\eta_{\rm m,fb}^{-1}$, which is ∼20 for most runs).

The first panel shows that the jet mass flux is independent of the feedback mass fraction. The jets in these runs have the same specific energy, so the same jet mass flux means the same momentum and energy flux, which implies a very similar cocoon propagation. With the lower feedback mass fraction, the BH accretes more to provide an equivalent level of feedback. This holds until the required accretion rate is much larger than the Bondi accretion rate, in which case the jet model will fail to self-regulate. That scenario is not within the parameter space we simulate here.

In the second panel, we vary the kinetic fraction by varying the jet temperature and velocity while keeping the total specific energy the same. The lower kinetic fraction run has most of the energy in a thermal component, isotropizing the cocoon essentially at the launch of the jet. Moreover, since its cocoon has never been in a momentum conserving phase, it does not reach far beyond the Bondi radius. It can clearly be seen in the last rows of Figs 4 and 5 that, although the isotropic component of the cocoon momentum flux matches the Bondi value at the Bondi radius in both the thermal and kinetic jets,

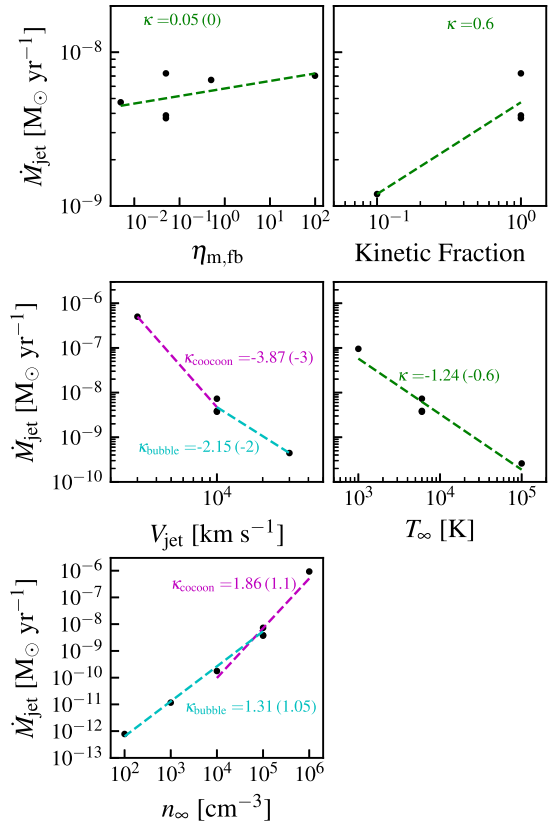

Figure 8. The dependence of the jet mass flux ($\dot{M}_{\rm jet}$) on the adopted jet model and background gas properties. The lines show power-law fits, with the index (κ) labelled. The number in the parenthesis is an estimate from the toy model and the fit to the cocoon gas-phase dependence in Fig. 7.

the cocoon momentum flux decays more steeply beyond the Bondi radius. As a result, much less energy is 'wasted' beyond the Bondi radius, so both the jet mass flux and BH accretion rates regulate to a lower value.

In the simulations where we vary the jet velocity (centre left panel), the cocoon density depends weakly on the jet velocity, as mentioned in Section 5.2. Therefore equation (19) ($z_{\rm iso} > R_{\rm Bondi}$) predicts a scaling of $\dot{M} \propto V_{\rm jet}^{-3}$, and equation (21) ($z_{\rm iso} < R_{\rm Bondi}$) predicts a scaling of $\dot{M} \propto V_{\rm jet}^{-2}$. These scaling relations roughly match what we see in Fig. 8. We plot the scaling relations fit to all of the runs with velocities $\gtrsim 10^4$ km s^{-1} (more elongated cocoon), and with velocities $\lesssim 10^4$ km s^{-1} (more bubble-like). As expected, the fits for the more elongated cocoon predict a steeper jet velocity dependence than the isotropic bubble case. It is also slightly steeper than what we predict from our simple model, but we re-emphasize that we are fitting a line to a small number of points and this result should be seen as a rough estimate.

When we vary the gas temperature (centre-right panel), we find a scaling relation $\dot{M}_{\rm jet} \sim T_\infty^{-1.2}$. This is qualitatively consistent but a bit steeper than our model (equations 21 and 19 with $\xi \sim 0$), which implies a scaling to $V_{\rm jet}$ with a power-law index of 0 to −0.18 (cocoon) or −0.5 to −0.7 (bubble).

Finally, when we vary the gas density (bottom left panel), the cocoon gas density depends on the background gas density as $n_c \propto n_\infty^\delta$ with $\delta \lesssim 0.9$. Therefore equations (21) and (19) predict $\dot{M}_{\rm jet} \propto n_\infty^\alpha$ with $\alpha \gtrsim 1.1$. We plot the scaling relations fit to the runs with density $\gtrsim 10^4$ km s^{-1} (more elongated cocoon), and with density $\lesssim 10^4$ km s^{-1} (more bubble-like). The first scenario has a similar scaling relation to our toy model. The latter case results in a somewhat steeper slope, which qualitatively agrees with our toy model but is steeper than predicted.

5.4 The growth of the black hole

We indicate the mean time-averaged BH accretion rate of each model in Table 1. The runs with the highest accretion rate are, unsurprisingly, the runs with the lowest feedback mass fraction ($\eta_{\rm m,\,fb} = 0.005$), the lowest relative specific energy (that is the lowest jet velocity, $V_{\rm jet} = 3000$ km s^{-1}), the highest background density ($n_\infty = 10^6$ cm^{-3}), and the lowest temperature ($T_\infty = 10^3 K$). They can all accrete at super-Eddington rates at their peak, reaching an accretion rate of $(10^{-6} - 10^{-5})$ M$_\odot$ yr^{-1} or (0.4–6) $\dot{M}_{\rm Edd}$ on average, where the reference Eddington accretion rate relates to the Eddington luminosity as $\dot{M}_{\rm Edd} \equiv L_{\rm Edd}/0.1c^2$ (although we remind readers that we are not treating radiative feedback in this work). In our surveyed parameter space, the presence of jet feedback suppresses the accretion rate below the Bondi rate by factors ranging from $\sim 2 \times 10^{-4}$ up to 0.7. Note that there is a strong time variability of the BH accretion rate and the resulting jet fluxes (see Fig. 2). We emphasize the strong dependence of the BH growth rate on the jet feedback efficiency, which is determined by $V_{\rm jet}$ and $\eta_{\rm m,\,fb}$, parametrize the sub-resolution physics. We only run the simulations for $<10^5$ yr, so none of the BHs grow significantly during the short periods covered by the simulations. Nevertheless, these results indicate that, for at least some of our model parameters, the BH could grow to very large masses in cosmologically short times if it continues to be surrounded by high-density gas.

We can express the ratio $\dot{M}_{\rm acc}/\dot{M}_{\rm Edd}$ using the scalings predicted by our toy model, normalized to the fiducial parameter choices, as

$$\frac{\dot{M}_{\rm acc}}{\dot{M}_{\rm Edd}} \sim 0.05 \left(\frac{\eta_{\rm m,BH}}{0.05}\right)^{-1} \left(\frac{V_{\rm jet}}{10^4\,{\rm km\,s^{-1}}}\right)^{-2\ {\rm to}\ -3} \times \left(\frac{n_\infty}{10^5\,{\rm cm^{-3}}}\right)^{1.1} \left(\frac{T_\infty}{10^4\,{\rm K}}\right)^{-0.6}, \quad (25)$$

where the exponent of $V_{\rm jet}$ ranges from 2 (for $r_{\rm iso} < r_{\rm Bondi}$) to 3 (for $r_{\rm iso} > r_{\rm Bondi}$). Assuming the separation of the two cases is roughly at $V_{\rm jet} \sim 10^4$ kms^{-1}, we plot the estimated BH accretion rate in Fig. 9. On top of the toy-model prediction, we indicate the results from our runs with circles coloured with their measured values, and they show a qualitative agreement. We also show a set of dashed lines showing the parameters for which the estimated time needed for a 100 M$_\odot$ BH to grow to 10^9 M$_\odot$ (t_{1e9}) is 10^7, 10^8, 10^9, and 10^{10} yr. Since we only performed simulations for a single BH mass, 100 M$_\odot$, in this study, this requires extrapolating the time-averaged accretion rates to higher BH masses. The calculation of t_{1e9} assumes $\dot{M}_{\rm acc} \propto M_{\rm acc}^2$ (corresponding to a fixed fraction of the Bondi rate, with fixed background gas properties) throughout the evolution. This is motivated by the $M_{\rm acc}$ dependence of $\dot{M}_{\rm jet}$ predicted in our toy model (see equations 19 and 21) but will be left for future study to verify with simulations with different BH masses. For a less optimistic estimate, the calculation of t_{1e9}^E instead assumes $\dot{M}_{\rm acc} \propto M_{\rm acc}$ (corresponding to a fixed fraction of the Eddington rate) throughout the evolution. Given the assumptions above and the estimated accretion rate of each case at $\dot{M}_{\rm acc} = 100$ M$_\odot$, part of the parameter space can have a 100 M$_\odot$ BH growing to a 10^9 M$_\odot$ SMBH at high redshift. We emphasize that these are crude estimations. The underlying assumptions of a fixed fraction of Bondi accretion and the constant background gas properties are subject to verification in future work.

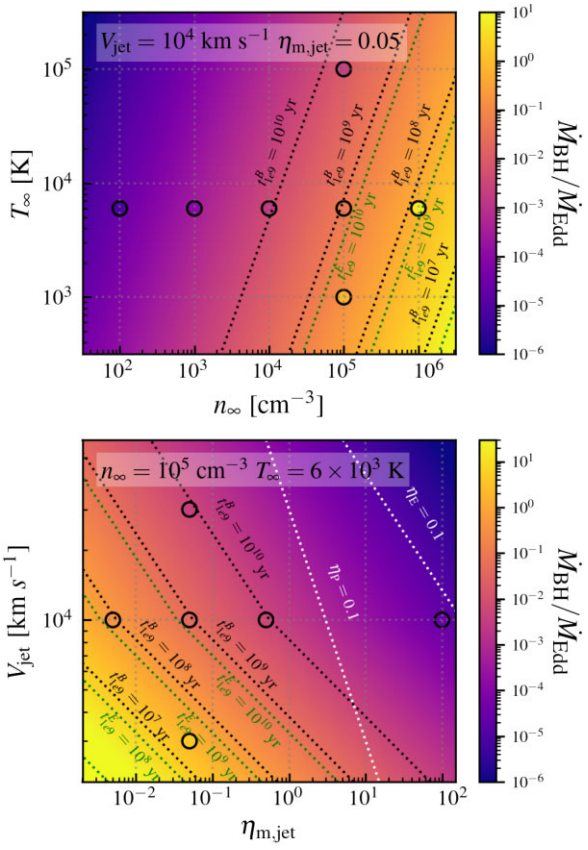

Figure 9. The predicted $\dot{M}_{\rm acc}/\dot{M}_{\rm Edd}$ from the scaling of our toy model, assuming a normalization to the fiducial runs. Runs with low background gas temperature (T_∞), high background gas density (n_∞), low jet velocity ($V_{\rm jet}$), or low feedback mass fraction ($\eta_{\rm m,\,jet}$) result in super-Eddington accretion. We also labelled with white dotted lines where the momentum efficiency ($\eta_{\rm p}$) and energy efficiency ($\eta_{\rm E}$) each equal to 0.1. The results from the simulations are shown as circles, coloured with the measured value. They show a qualitative agreement with the toy model. The dashed lines show the parameters for which the estimated time required for a 100 $M_\odot$ BH to grow to 10^9 $M_\odot$ (t_{1e9}) is 10^7, 10^8, 10^9, and 10^{10} yr. The calculation of t^B_{1e9} assumes $\dot{M}_{\rm acc} \propto M^2_{\rm acc}$ (black, fixed fraction of Bondi rate with fixed background gas properties) throughout the evolution. The calculation of t^E_{1e9} adopts a less optimistic extrapolation of the BH accretion rate.
$\dot{M}_{\rm acc} \propto M_{\rm acc}$ (red, fixed fraction of the Eddington rate) throughout the evolution.

5.5 Jet cocoon height

As we saw in Fig. 5, all of the jets simulated in this paper reach only to ∼0.1 pc. Some of the cases isotropize at even shorter heights. We emphasize that this is ultimately the result of our choice of a 100 $M_\odot$ BH. Supposing that our toy model holds for any BH mass (subject to verification in future work), we can combine equations (12) and (25) (with $\dot{M}_{\rm acc}$ dependence) as

$$z_{\rm iso} \propto M_{\rm acc} V_{\rm jet}^{-1.5\ to\ -2} T_\infty^{-0.3}. \quad (26)$$

Therefore, the isotropic height scales roughly with the BH mass. Besides, a jet cocoon propagates until reaching a height where the integrated cooling rates within the jet cocoon balance the jet energy fluxes. Given that most of the cooling happens at the mixing layer, we can write down

$$\dot{E}_{\rm jet} \propto z^2_{\rm max} \delta\ell n^2_\infty \Lambda(T_\infty), \quad (27)$$

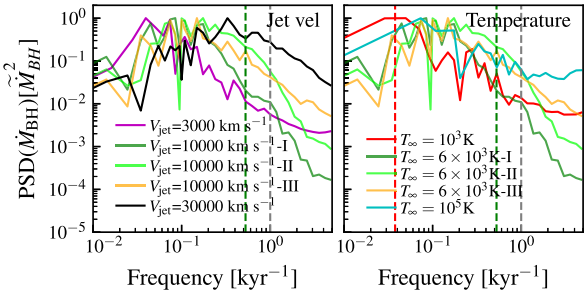

Figure 10. The normalized (divided by the maximum value) power spectrum of the BH accretion history (from the first panel of Fig. 2). The green and red vertical lines are the free-fall time at the Bondi radius for 6×10^3 K and $\times 10^3$ K gas. The corresponding value for $\times 10^5$ K is outside the plotted range (right end). The grey line is the viscous time-scale of the α-disc. The lower jet velocity run results in a more elongated cocoon, which reaches a larger distance, and has longer term variability. The run with cooler background gas also has a larger Bondi radius, so the BH accretion rate also has longer term variability.

where $\delta\ell$ is the mixing layer thickness. Accordingly, the maximum height a jet cocoon reaches, $z_{\rm max} \propto M_{\rm acc}$, again, scales roughly with the BH mass. Our result for a 100 $M_\odot$ BH, therefore, does not conflict with observations of narrow jet cocoons reaching kpc scales produced by an SMBH.

Moreover, a high density is unrealistic to stay constant to such larger radii. For more massive systems, jets will propagate into a lower density, while getting fuelled by the central more dense gas. From equation (10), this can make the jet more collimated by keeping $\dot{M}_{\rm jet}$ constant while lowering $\rho_{\rm c}$ (this should not be confused with our earlier statement that a higher background density will result in a more collimated jet, which is a result of self-regulation as the jet flux scales superlinearly with the background density).

5.6 Jet duty cycle

Besides regulating the BH accretion rate and jet mass flux, the various jet models and background gas properties also affect the feedback cycle period. A run with a more elongated jet cocoon that propagates to a larger distance will result in longer term variability in the accretion rate. This can be seen in the left-hand panel of Fig. 10, where we quantify the normalized (i.e. divided by its maximum value) power spectrum of the BH accretion rate in the runs with different velocities. We clearly see that the slower the jet velocity, the more elongated the jet cocoon becomes and the more the power spectrum shifts to longer periods (lower frequencies). The reason for this behaviour is simply that, when the jet reaches a larger distance, the time-scale of the regulation (i.e. the free-fall time) becomes longer.

Similarly, changing the gas temperature also impacts the distance that the cocoon reaches. In the right-hand panel of Fig. 10, we see that the higher temperature run, which has the smaller Bondi radius, has a power spectrum shifted to shorter periods.

6 DISCUSSION

6.1 The surveyed feedback efficiency

In this work, we parametrize an AGN feedback model with $V_{\rm jet}$, $T_{\rm jet}$, and $\eta_{\rm m,\,jet}$. Effectively we could re-parametrize each model with $V_{\rm jet}$ and the feedback energy and momentum efficiencies, which are

defined as

$$\eta_{\rm p} \equiv \frac{\dot{P}_{\rm jet}}{\dot{M}_{\rm acc}c} = \frac{\dot{M}_{\rm jet}V_{\rm jet}}{\dot{M}_{\rm acc}c}$$
$$\eta_{\rm E} \equiv \frac{\dot{E}_{\rm jet}}{\dot{M}_{\rm acc}c^2} = \frac{\dot{M}_{\rm jet}V_{\rm jet}^2}{2\dot{M}_{\rm acc}c^2}. \quad (28)$$

We effectively did a very broad survey of the energy efficiency $\eta_{\rm E}$ from $2.7\times10^{-6}-0.055$, and momentum fluxes $\eta_{\rm P}$ from $1.6\times10^{-4}-3.3$. All our runs and the scaling from our toy model can be re-parametrized with these efficiencies (as labelled in Table 1 and Fig. 9). However, we found the current labelling results in a simpler scaling in the model, as they are the relevant variables in our toy model.

We emphasize that ($V_{\rm jet}$, $T_{\rm jet}$, $\eta_{\rm m,\,jet}$) or ($V_{\rm jet}$, $\eta_{\rm p}$, $\eta_{\rm E}$) are merely parametrizing our ignorance of the sub-resolution physics. In the literature, the momentum and energy efficiencies $\eta_{\rm p}$ and $\eta_{\rm E}$ are often considered within one dex above and below 0.1, and often with a maximum value around 1, depending on the BH spin and accretion disc model (e.g. De Villiers et al. 2005; Tchekhovskoy, Narayan & McKinney 2011; McKinney, Tchekhovskoy & Bland ford 2012; Sadowski et al. 2016). However, these values are often measured in GRMHD simulations at the BH horizon scale, with $\dot{M}_{\rm acc}$ measured right around the black horizon. The Bondi solution has a constant $\dot{M}_{\rm acc}$ across the wide radial range within the Bondi radius, but mass-loss to winds and outflows generally result in $\dot{M}_{\rm acc}$ decreasing monotonically towards inner radii. This lowers both the effective jet energy and momentum efficiencies, as the BH accretion rate is much smaller than the $\dot{M}_{\rm acc}$ calculated at the resolution scale. For instance, the typical scaling of $\dot{M}\propto r^{1/2}$ found in radiation-hydrodynamical simulations (e.g. Guo et al. 2022; Hu et al. 2022, and references therein) implies effectively $\sim$3 orders of magnitude suppression of the efficiency in our definition, given the 6 orders of magnitude from our sink radius to the BH horizon. Earlier work also predicts a scaling of $\dot{M}\propto r^{0.4-0.8}$, which can be slightly steeper (Yuan & Narayan 2014). Moreover, how the flux of the jet varies as it reaches our launching scale is subject to the sub-grid gas properties, which change the thermalization rate of kinetic energy, cooling physics, and kinematics. The range of these efficiencies can possibly be larger than most studies in the literature cover.

Given the above complexities, instead of having a set of runs attempting to parametrize the possible effective efficiencies at our jet launching scale given a certain efficiency measured at the BH horizon scale, we instead intentionally cover a very wide possible parameter space at our jet launching scale. The relations of these runs to a relativistic jet at the black-horizon scale and the jet propagation in the scales in between will be left for a future study. Our chosen set of runs may also be more suitable to validate our toy model, as they cover orders of magnitude ranges for each parameter.

6.2 Comparison with previous works

Regan et al. (2019) used the adaptive mesh refinement (AMR) hydrodynamics code ENZO to investigate feedback from bipolar jets, expected to be produced during super-Eddington accretion episodes, focusing on how the jet feedback impacts BH growth. They found that the jets periodically evacuate the central $\sim$0.1pc region, and accretion then resumes after a free-fall time. Overall, we here find a similar behaviour, although there are several differences between our setups and our results. Regan et al. (2019) utilize a cosmological simulation, and adopt an initial seed BH mass of 16 000 $M_\odot$, with an initial accretion rate of $\sim10^{-2}$ $M_\odot$ yr^{-1}, and find that the time-averaged accretion rate always stays below the Eddington value. Also, once the gas is heated by the jet, they do not resolve the Bondi radius, and adopt a modified Bondi accretion rate. By comparison, we here use an initially uniform and static cloud, and examine a $>$100 times lower BH mass, $>$100 times lower accretion rate, and a $>$100 times higher spatial resolution, such that the Bondi radius remains resolved at all times. We find that super-Eddington accretion is possible, which may be explained by the different parameter choices and/or differences in the details in the shapes of the jet-driven cocoons. Another difference between our studies is that we examine the cocoon evolution in greater detail and offer a physical interpretation of its shape and size, as a function of jet and background gas parameters.

Park & Ricotti (2011) studied a similar problem regarding accretion on to a low-mass BH, but with radiative feedback instead of the mechanical jet feedback explored here. They obtain a scaling of the time-averaged BH accretion rate with background gas properties ($\dot{M}\propto T_\infty^{5/2}$ for $n_\infty\geq10^5$ cm^{-3} and $\dot{M}\propto T_\infty^{5/2}n_\infty^{1/2}$ for $n_\infty<10^5$ cm^{-3}), which are different from ours. The primary reason is that the radiative feedback they implemented inflates a roughly constant temperature bubble around the BH, which is in pressure equilibrium with the surrounding cold gas. This is very different from the cocoon we see inflated by jet feedback, where the cocoon has a more complicated shape as discussed in Section 4. Park & Ricotti (2011) also found a feedback cycle with a well-defined period, while we have much more complicated cycles. This can arise from the more anisotropic turbulent gas distribution due to the jetted feedback or the more complex geometry of the outflows and accretion. The fact that we are using 3D simulations, while Park & Ricotti (2011) used 1D and 2D simulations, could also contribute to the difference. Overall, the time-averaged accretion rate in Park & Ricotti (2011) was found to always remain below the Eddington rate, whereas we here find super-Eddington accretion in many cases. This suggests that jet feedback may be a lesser obstacle to BH growth than radiative feedback.

Takeo et al. (2020) also studied a similar problem with different BH masses (10 and 10^5 $M_\odot$) and with wider AGN winds on top of radiative feedback. They focused on the 'hyper-Eddington' regime, such that the Bondi rate exceeds the Eddington rate by several orders of magnitude. In practice, they considered either a much higher BH mass or a much higher background gas density than in our study. They showed that under these conditions, the resulting accretion rate can remain close to the Bondi accretion rate and reach the prescribed hyper-Eddington values after around a dynamical time, when the radiative feedback becomes less important. They also found that the accretion rate is insensitive to the feedback mass fraction of the mechanical feedback. These latter findings are qualitatively similar to what we see in our simulations with the AGN jet, despite different initial velocity and initial open-angle. They also see momentum conserving wind propagation (constant velocity) all the way to beyond Bondi radius, qualitatively similar to what we see in our lower velocity jets, which is also expected in our toy model. Given the difference in the feedback form, BH mass, run time, and background Bondi accretion rate, more quantitative comparisons would be difficult.

It is worth also comparing our results with the jets in larger scale galaxy simulations, e.g. those presented in Su et al. (2021). A similar qualitative result was found in those galaxy scale studies, namely that heavier jets result in much narrower jet cocoons which propagate much farther. The toy model describing the jet propagation presented in Section 4 also works on galaxy scales with a much more massive BH and lower gas density. One important difference is the relative strength of radiative cooling, which operates more

rapidly in the current simulations. Here, we find significant cooling at the contact discontinuity between the shocked jet material and the shocked ambient medium, whereas cooling on the cluster and galaxy scale is slower and occurs mostly in gas which is not shock-heated.

Massonneau et al. (2022) also examined the impact of jet feedback on BH growth on larger (∼kpc scales), in a 10^{11} $M_\odot$ dark matter halo and found that mildly super-Eddington accretion is possible. They found that weaker super-Eddington jets allow for more rapid BH growth through more frequent super-Eddington episodes, and also that weaker jet feedback efficiency leads to larger BH masses, which are consistent with our findings.

6.3 Connection to other scales

Part of the motivation of this work, where we perform intermediate-scale simulations, is to provide insight in connecting galaxy scale simulations and GRMHD simulations that can resolve the accretion disc. Depending on the galaxy size and the numerical method, the finest resolution of the former case is at best ∼0.1 pc, and generally much lower (e.g. Wetzel et al. 2016; Su et al. 2018; Wheeler et al. 2019; Massonneau et al. 2022). The outer boundary of the latter case is at most $\sim 1000 r_g$ (r_g is the gravitational radius; e.g. Lalakos et al. 2022), which is roughly $10^{-8}(M_{\rm acc}/100\,{\rm M}_\odot)$ pc, implying a $\gtrsim 7$ order of magnitude gap for the BH mass we model here. Our simulation, with its outer boundary at roughly 0.2 pc and a maximum resolution of $\sim 10^{-4}$ pc fits between these scales, although we note that we are still far from $\sim 1000 r_g$.

Unless using GRMHD simulations, which resolve the gravitational radius, AGN jets are not self-consistently launched but are implemented instead with sub-grid prescriptions. Effectively these sub-grid 'jet models' attempt to inject the fluxes of a'cocoon' inflated by a jet launched on an even smaller scale. Therefore, even identical jet energy, momentum, and mass fluxes can produce different physical behaviour when launched on different scales. This work provides a framework for coarse-graining jet models launched on a smaller scale to the resolution scale of galaxy simulations. The toy model described in Section 4 and verified in our simulations describes how the cocoon energy, momentum, and mass flux should scale as a function of radius. The scalings can be incorporated into simulations on different scales for the same sub-grid jet model.

Effectively, given a certain estimated density (n_∞) and temperature (T_∞) around a BH, and a jet model ($V_{\rm jet}$) on a small scale, $r_{\rm small}$, equation (22) can roughly determine whether $z_{\rm iso}$ is larger or smaller than $R_{\rm Bondi}$. Depending on which side it falls, the resulting time-averaged $\dot{M}_{\rm jet}$ can be estimated through equation (19) or equation (21). Note that we also need the ζ, ξ, and δ values from the fit results in Fig. 7. Assuming we want to find the effective cocoon property at a given larger radius, $r_{\rm large}$, the cocoon expansion either follows equations (8) and (9) (if $r_{\rm large} < r_{\rm iso}$) or equation (14) (if $r_{\rm large} > r_{\rm iso}$). Therefore, with the values n_∞, T_∞, $V_{\rm jet}$, ζ, ξ, δ, and $\dot{M}$, we find the corresponding cocoon expansion velocity at a specific radius $r_{\rm large}$, which can be used as an 'effective' coarse-grained jet model at that scale. The aforementioned implementation should, of course, be explicitly tested in galaxy-scale simulations. Indeed, besides the effective velocities, there is also the complexity of an 'effective' jet model, including the temperature, time variability, gas cooling, and the exact sampling of the velocity distribution while launching the feedback. We leave a thorough investigation of these issues, and the construction of a full sub-grid jet recipe, to future work.

6.4 Limitations of this work and future prospects

We emphasize that we have deliberately considered an idealized setup, with an initially static cloud with a uniform density and temperature. In reality, the gas surrounding the BH could be highly turbulent with a non-zero net angular momentum. In addition, in a very inhomogeneous environment, the stochastic capture of certain ultradense clumps with low relative velocity might play a very important role (Shi et al. 2023).

We also consider only one BH mass (see e.g. Regan et al. 2019; Takeo et al. 2020; Massonneau et al. 2022, for similar studies with larger BHs). Moreover, this work does not include magnetic fields, conduction, viscosity, and other plasma physics, which may be important on these scales. In particular magnetic fields could play a role in collimating jets, especially for the Poynting flux-dominated relativistic case (e.g. Bromberg et al. 2014). The jet model we considered in this work is in the limit where a jet becomes more mass-loaded after propagating to a certain scale that we can resolve. Therefore, we do not expect such an effect to be significant in our case, but it is subject to further verification.

For the feedback itself, we only include jet feedback in this work for simplicity, ignoring any radiative feedback (e.g. Park & Ricotti 2011; Regan et al. 2019; Takeo et al. 2020), which may also play an important role in the BH's neighbourhood. Due to the limitations of non-relativistic hydrodynamics, we also limit the jet velocity to $\lesssim 30000\,{\rm km\,s^{-1}}$. As a relativistic jet propagates further from the gravitational radius, it can gradually slow down as more gas gets entrained. Moreover, when taking into account the self-consistently launched jet properties from GRMHD simulations slightly away from the jet axis, the average jet velocity also gets much lower (Chatterjee et al. 2019). The adopted velocities should be reasonable at the jet launching scale of our simulations but might not cover the whole possible parameter space in more extreme circumstances. We also did not explore models with wider opening-angle AGN winds (e.g. Takeo et al. 2020). Cosmic rays might be another critical aspect of AGN feedback as well (Su et al. 2020, 2021; Wellons et al. 2022), but are not included here. We will explore these aspects in future work.

We also note that we only focus on the BH growth due to gas accretion. There could be many other possible channels for BH growth, like runaway mergers between stellar-mass BHs (e.g. Kroupa et al. 2020).

7 CONCLUSION

In this work, we utilized high-resolution hydrodynamic simulations of 0.4–1.6 pc boxes with uniform initial density and temperature to study jet propagation and its effect on BH accretion on to a 100 $M_\odot$ BH in low metallicity dense gas. We found that the isotropic component of the cocoon momentum flux regulates the BH accretion and the mass, momentum, and energy flux from the AGN jet. We summarize our major conclusions as follows:

(i) After a jet is launched, it inflates a jet cocoon filled with a hot reverse shock-heated turbulent gas and a much cooler gas phase at the mixing layer with the surrounding gas.

(ii) At launch, a jet cocoon will propagate, conserving the momentum in the jet direction while continuously broadening itself through thermal pressure in the lateral directions. Eventually, the cocoon expands laterally and the propagation in the jet direction slows down. If the jet cocoon propagates to a sufficiently large radius,

it eventually evolves into a quasi-spherical bubble. After that, the cocoon propagates isotropically in an energy-driven scenario.

(iii) Depending on the jet and background gas properties, the inflated cocoon either isotropizes beyond the Bondi radius (retaining an elongated shape), or inside the Bondi radius (becoming spherical bubble-like).

(iv) In either case, the isotropic component of the cocoon momentum flux (roughly twice the lateral momentum flux if the cocoon is elongated) on average matches the inflow momentum flux at the Bondi radius, assuming a Bondi-accretion scenario. This, in turn, regulates the BH accretion.

(v) We presented a toy model based on this picture which results in a scaling of the BH accretion rate that roughly matches the rate found in the simulations.

(vi) The lower the jet velocity and the higher the background gas density, the more elongated the jet cocoon.

(vii) In addition to the average BH accretion rate and jet mass flux, the different jet model and background gas properties also affect the accretion history variability. A jet model that produces an elongated cocoon propagates to a larger distance and produces longer-time-scale variability, while smaller and more spherical bubble-like cocoons produce shorter-time-scale variability. Higher T_∞ (smaller $R_{\rm Bondi}$) also leads to more short-time-scale variability.

(viii) The runs with the highest accretion rates are those with the lowest feedback mass fraction ($\eta_{\rm m,\,fb} = 0.005$), the lowest specific energy or jet velocity ($V_{\rm jet} = 3000\ {\rm km\,s^{-1}}$), the highest density ($n_\infty = 10^6\ {\rm cm^{-3}}$), or the lowest temperature ($T_\infty = 10^3$ K). They, on average, have super-Eddington accretion, $\dot{M}_{\rm acc} \sim 0.4 - 6\dot{M}_{\rm Edd}$. In our surveyed parameter space, the presence of AGN jets suppresses the Bondi accretion rate by factors from $\sim 2 \times 10^{-4}$ to 0.6.

In summary, this work shows how different jet models (and background gas properties) result in different cocoon properties and accretion rates. Our results suggest that at least initially, stellar-mass BHs in so-called atomic cooling haloes may be able to grow at rates well above the Eddington rate. Our study also suggests a prescription to link simulations on different scales (Section 6.3). Many caveats and unanswered questions remain (see Section 6.4) to be explored in future work.

ACKNOWLEDGEMENTS

We thank the anonymous referee for useful comments that helped improve the clarity of our manuscript. Numerical calculations were run on the Flatiron Institute cluster 'popeye' and 'rusty' and allocations TG-PHY220027 and TG-PHY220047 granted by the Engineering Discovery Environment (XSEDE) supported by the NSF. KS acknowledges support from the Black Hole Initiative at Harvard University, which is funded by grants from the John Templeton Foundation and the Gordon and Betty Moore Foundation, and support from Simons Foundation. GLB acknowledges support from the NSF (OAC-1835509, AST-2108470), a NASA TCAN award, and the Simons Foundation. ZH acknowledges support from NSF grant AST-2006176. RSS and CCH were supported by the Simons Foundation through the Flatiron Institute. CAFG was supported by NSF through grants AST-1715216, AST-2108230, and CAREER award AST-1652522; by NASA through grants 17-ATP17-0067 and 21-ATP21-0036; by STScI through grants HST-AR-16124.001-A and HST-GO-16730.016-A; by CXO through grant TM2-23005X; and by the Research Corporation for Science Advancement through a Cottrell Scholar Award.

DATA AVAILABILITY

The data supporting the plots within this article are available on reasonable request to the corresponding author. A public version of the GIZMO code is available at http://www.tapir.caltech.edu/~phopkins/Site/GIZMO.html.

REFERENCES

Alvarez M. A., Wise J. H., Abel T., 2009, ApJ, 701, L133
Anglés-Alcázar D., Davé R., Faucher-Giguère C.-A., Özel F., Hopkins P. F., 2017, MNRAS, 464, 2840
Anglés-Alcázar D. et al., 2021, ApJ, 917, 53
Begelman M. C., Cioffi D. F., 1989, ApJ, 345, L21
Bîrzan L., Rafferty D. A., McNamara B. R., Wise M. W., Nulsen P. E. J., 2004, ApJ, 607, 800
Bondi H., 1952, MNRAS, 112, 195
Bosman S. E. I., 2022, Zenodo
Bourne M. A., Sijacki D., 2017, MNRAS, 472, 4707
Bradford J. D., Geha M. C., Greene J. E., Reines A. E., Dickey C. M., 2018, ApJ, 861, 50
Bromberg O., Granot J., Lyubarsky Y., Piran T., 2014, MNRAS, 443, 1532
Chatterjee K., Liska M., Tchekhovskoy A., Markoff S. B., 2019, MNRAS, 490, 2200
Cho H., Narayan R., 2022, ApJ, 932, 97
De Villiers J.-P., Hawley J. F., Krolik J. H., Hirose S., 2005, ApJ, 620, 878
Dickey C. M., Geha M., Wetzel A., El-Badry K., 2019, ApJ, 884, 180
Dubois Y., Devriendt J., Slyz A., Teyssier R., 2010, MNRAS, 409, 985
Fabian A. C., 2012, ARA&A, 50, 455
Gaspari M., Brighenti F., Temi P., 2012, MNRAS, 424, 190
Greene J. E., Ho L. C., Ulvestad J. S., 2006, ApJ, 636, 56
Guo F., 2015, ApJ, 803, 48
Guo M., Stone J. M., Kim C.-G., Quataert E., 2022, ApJ, preprint (arXiv:2211.05131)
Hickox R. C., Alexander D. M., 2018, ARA&A, 56, 625
Hopkins P. F., 2015, MNRAS, 450, 53
Hopkins P. F., Quataert E., 2011, MNRAS, 415, 1027
Hopkins P. F., Torrey P., Faucher-Giguère C.-A., Quataert E., Murray N., 2016, MNRAS, 458, 816
Hopkins P. F. et al., 2018, MNRAS, 480, 800
Hu H., Inayoshi K., Haiman Z., Quataert E., Kuiper R., 2022, ApJ, 934, 132
Inayoshi K., Haiman Z., Ostriker J. P., 2016, MNRAS, 459, 3738
Inayoshi K., Visbal E., Haiman Z., 2020, ARA&A, 58, 27
Jiang Y.-F., Stone J. M., Davis S. W., 2014, ApJ, 796, 106
Krause M., 2003, A&A, 398, 113
Kroupa P., Subr L., Jerabkova T., Wang L., 2020, MNRAS, 498, 5652
Lalakos A. et al., 2022, ApJ, 936, L5
Li Y., Bryan G. L., 2014, ApJ, 789, 54
Li Y., Bryan G. L., Ruszkowski M., Voit G. M., O'Shea B. W., Donahue M., 2015, ApJ, 811, 73
López-Cámara D., De Colle F., Moreno Méndez E., 2019, MNRAS, 482, 3646
McKinney J. C., Tchekhovskoy A., Bland ford R. D., 2012, MNRAS, 423, 3083
Manzano-King C. M., Canalizo G., Sales L. V., 2019, ApJ, 884, 54
Martizzi D., Quataert E., Faucher-Giguère C.-A., Fielding D., 2019, MNRAS, 483, 2465
Massonneau W., Volonteri M., Dubois Y., Beckmann R. S., 2022, preprint (arXiv:2201.08766)
Mezcua M., Lobanov A. P., 2011, Astron. Nachr., 332, 379
Mezcua M., Farrell S. A., Gladstone J. C., Lobanov A. P., 2013a, MNRAS, 436, 1546
Mezcua M., Roberts T. P., Sutton A. D., Lobanov A. P., 2013b, MNRAS, 436, 3128

Mezcua M., Roberts T. P., Lobanov A. P., Sutton A. D., 2015, MNRAS, 448, 1893
Mezcua M., Civano F., Marchesi S., Suh H., Fabbiano G., Volonteri M., 2018a, MNRAS, 478, 2576
Mezcua M., Kim M., Ho L. C., Lonsdale C. J., 2018b, MNRAS, 480, L74
Mezcua M., Suh H., Civano F., 2019, MNRAS, 488, 685
Milosavljević M., Bromm V., Couch S. M., Oh S. P., 2009, ApJ, 698, 766
Nyland K., Marvil J., Wrobel J. M., Young L. M., Zauderer B. A., 2012, ApJ, 753, 103
Nyland K. et al., 2017, ApJ, 845, 50
Park K., Ricotti M., 2011, ApJ, 739, 2
Penny S. J. et al., 2018, MNRAS, 476, 979
Prasad D., Sharma P., Babul A., 2015, ApJ, 811, 108
Regan J. A., Downes T. P., Volonteri M., Beckmann R., Lupi A., Trebitsch M., Dubois Y., 2019, MNRAS, 486, 3892
Reines A. E., Deller A. T., 2012, ApJ, 750, L24
Reines A. E., Plotkin R. M., Russell T. D., Mezcua M., Condon J. J., Sivakoff G. R., Johnson K. E., 2014, ApJ, 787, L30
Ruszkowski M., Yang H.-Y. K., Zweibel E., 2017, ApJ, 834, 208
Sadowski A., Narayan R., McKinney J. C., Tchekhovskoy A., 2014, MNRAS, 439, 503
Sadowski A., Lasota J.-P., Abramowicz M. A., Narayan R., 2016, MNRAS, 456, 3915
Sbarrato T., Ghisellini G., Giovannini G., Giroletti M., 2021, A&A, 655, A95
Sbarrato T., Ghisellini G., Tagliaferri G., Tavecchio F., Ghirlanda G., Costamante L., 2022, A&A, 663, A147
Shakura N. I., Sunyaev R. A., 1973, A&A, 500, 33
Shi Y., Kremer K., Grudić M. Y., Gerling-Dunsmore H. J., Hopkins P. F., 2023, MNRAS, 518, 3606
Springel V., Di Matteo T., Hernquist L., 2005, MNRAS, 361, 776
Su K.-Y. et al., 2018, MNRAS, 480, 1666
Su K.-Y. et al., 2020, MNRAS, 491, 1190
Su K.-Y. et al., 2021, MNRAS, 507, 175
Takeo E., Inayoshi K., Mineshige S., 2020, MNRAS, 497, 302
Tchekhovskoy A., Narayan R., McKinney J. C., 2011, MNRAS, 418, L79
Torrey P. et al., 2020, MNRAS, 497, 5292
Volonteri M., Habouzit M., Colpi M., 2021, Nat. Rev. Phys., 3, 732
Webb N. et al., 2012, Science, 337, 554
Weinberger R., Ehlert K., Pfrommer C., Pakmor R., Springel V., 2017, MNRAS, 470, 4530
Weinberger R. et al., 2022, MNRAS, preprint (arXiv:2211.11771)
Wellons S. et al., 2022, MNRAS, preprint (arXiv:2203.06201)
Wetzel A. R., Hopkins P. F., Kim J.-h., Faucher-Giguère C.-A., Kereš D., Quataert E., 2016, ApJ, 827, L23
Wheeler C. et al., 2019, MNRAS, 490, 4447
Wrobel J. M., Ho L. C., 2006, ApJ, 646, L95
Wrobel J. M., Greene J. E., Ho L. C., Ulvestad J. S., 2008, ApJ, 686, 838
Yang H.-Y. K., Reynolds C. S., 2016, ApJ, 818, 181
Yang H. Y. K., Sutter P. M., Ricker P. M., 2012, MNRAS, 427, 1614
Yuan F., Narayan R., 2014, ARA&A, 52, 529

APPENDIX: RESOLUTION STUDY AND THE VARIATIONS OF ACCRETION MODELS

Fig. A1 summarizes the effects of different choices of sink radius and alpha disc model on BH accretion rates $\dot{M}_{\rm acc}$ under different resolutions. All the runs match our fiducial parameter choice ($\zeta_{\rm m,\,fb} = 0.05$, $V_{\rm jet} = 10^4\,{\rm km\,s^{-1}}$, $n_\infty = 10^5{\rm cm^{-3}}$, and $T_\infty = 10^4 K$). The first three rows shows the moving-averaged (over 10 kyr) value to the point at the specific time of the simulation. Most simulations are run with different variations of the random component to quantify the stochastic effect (different lines in the same colour). A list of different simulations is summarized in Table A1.

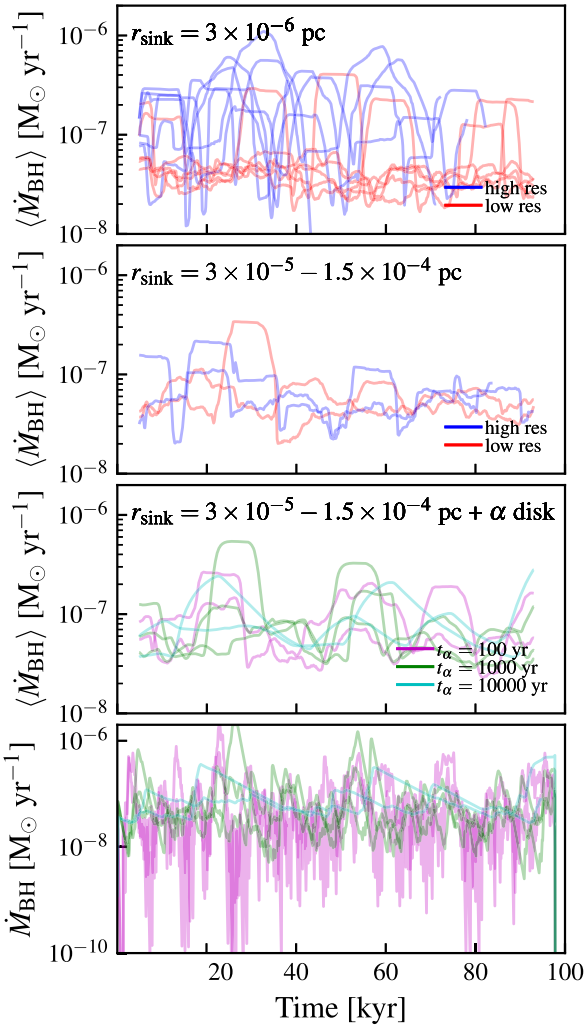

Figure A1. The effects of different choices of sink radius and alpha disc models on BH accretion rate $\dot{M}_{\rm acc}$ under different resolutions. The first three rows show the moving-time-averaged (10 kyr) accretion rates for a range of sink radii, resolutions, and alpha disc parameters. To explore stochastic variations, we run simulations are run with different variations of the random component (different lines in the same colour). With the smallest sink radius (0.003 mpc), the random number variations result in a factor of 2–3 span in the final results, indicating that stochastic effects are significant. The higher resolution runs also result in a factor of 2–3 higher $\dot{M}_{\rm acc}$. The runs with a larger sink radius have slightly better convergence and smaller stochastic effects ($\lesssim 2$). The model with alpha discs and different viscous time-scales also have accretion rates with differences within a factor of 2, well within the stochastic range. The bottom panel shows the real-time $\dot{M}_{\rm acc}$ of the runs with different viscous time-scales. A shorter viscous time-scale results in shorter-term variations.

With the smallest sink radius (3×10^{-6} pc), the stochastic effects result in a factor of 2–3 span in the final results indicating a substantial stochastic effect. The higher resolution runs also result in a factor of 2–3 higher $\dot{M}_{\rm acc}$. The small sink radius also leads to the occasional formation of a discy structure right around the BH at high resolution, which partially contributes to the more significant resolution dependence. Given that we do not have the proper resolution and physics to model the accretion disc explicitly, we shift to a larger sink radius and put in a subgrid α-disc model as described in the main paper.

Table A1. Physics variations (run at highest resolution) explored in this appendix.

Model	ΔT kyr	Box size pc	$m_{\rm g}^{\rm max}$ $M_\odot$	$m_{\rm jet}$ $M_\odot$	Accretion model $r_{\rm sink}$ 10^{-3} pc	t_α kyr
$r_{\rm sink} = 3 \times 10^{-6}$ pc						
High res	40–80	0.4	1.7e-7	3e-8	0.003	No
Low res	100	0.4	1.4e-6	1e-7	0.003	No
$r_{\rm sink} = 3 \times 10^{-5} - 1.5 \times 10^{-4}$ pc						
High res	100	0.4	1.7e-7	3e-8	0.03−0.15	No
Low res	100	0.4	1.4e-6	1e-7	0.03−0.15	No
$r_{\rm sink} = 3 \times 10^{-5} - 1.5 \times 10^{-4}$ pc $+ \alpha$ disc						
100 yr	100	0.4	1.4e-6	1e-7	0.03–0.15	0.1
1000 yr	100	0.4	1.4e-6	1e-7	0.03–0.15	1
10000 yr	100	0.4	1.4e-6	1e-7	0.03–0.15	10

Note. This is a partial list of simulations that explore resolution and numerical parameter choice. All simulations are run with ($\zeta_{\rm m,\,fb} = 0.05$, $V_{\rm jet} = 10^4$ km s^{-1}, $n_\infty = 10^5$ cm^{-3}, and $T_\infty = 10^4 K$).Columns list: (1) Model name: The naming of each model starts with the feedback mass fraction, followed by the jet velocity in km s^{-1} for kinetic jet or jet temperature in K for thermally dominant jets. The final two numbers label the background gas density in cm^{-3} and temperature in K. (2) ΔT: Simulation duration. (3) Box size of the simulation.(4) $m_{\rm g}^{\rm max}$: The highest mass resolution.(5) $m_{\rm jet}^{\rm max}$: The mass resolution of the spawned jet particles.(6) $r_{\rm sink}$: Sink radius in 10^{-3} pc.(7) t_α: Viscous time-scale for alpha disc in kyr.

The runs with a larger sink radius ($3 \times 10^{-5} - 1.5 \times 10^{-4}$ pc)[5] have a slightly smaller dependence on resolution and smaller stochastic effects (everything within $\lesssim$2), partially due to the suppression of an artificial discy structure at very small radius. This level of difference (even the small sink radius runs) is smaller than the difference caused by most of the physics variations Figs 2 and 8. In our production run, we adopt the larger sink radius (3×10^{-5} to 1.5×10^{-4} pc). Given the smaller resolution dependence with this sink radius, we try to match the lower resolution for most of our physical variations for lower computational cost.

The models with alpha disc and different viscous time-scales also result in differences within a factor of two, within the stochastic range, and roughly have the same accretion rates as the runs without an alpha disc. The final row of Fig. A1 shows the real-time $\dot{M}_{\rm acc}$ of the runs with different viscous time-scales. Shorter time-scale results in a shorter-term variation. We adopt $t_\alpha = 1000$ yr in our productive runs according to an estimate of the viscous time-scale at the sink radius we choose (see Section 2).

[5]The sink radius is set to be a radius from the BH enclosing 96 'weighted' neighbourhood gas particles but capped to be within (3×10^{-5} to 1.5×10^{-4} pc).

This paper has been typeset from a TEX/LATEX file prepared by the author.